Computer Modeling in Engineering & Sciences

Tech Science Press

https://doi.org/10.32604/cmes.2026.084696

ARTICLE

Predicting the Compressive Strength of Sustainable Concrete Containing Recycled Aluminum Beverage Cans Crumb Using Machine Learning Techniques

Manish Kewalramani[1], Refka Ghodhbani[2], Arsalan Mahmoodzadeh[3,*], Abdulaziz Alghamdi[4], Faten Khalid Karim[5], Abed Alanazi[6], Abdullah Alqahtani[6], Shtwai Alsubai[6] and Mounir Ltifi[7]

[1]Department of Civil Engineering, College of Engineering, Abu Dhabi University, Abu Dhabi, United Arab Emirates
[2]Department of Civil Engineering, College of Engineering, Northern Border University, Arar, Saudi Arabia
[3]Center of Research and Strategic Studies, Lebanese French University, Erbil, Iraq
[4]Department of Civil Engineering, Faculty of Engineering, University of Tabuk, Tabuk, Saudi Arabia
[5]Department of Computer Sciences, College of Computer and Information Sciences, Princess Nourah bint Abdulrahman University, Riyadh, Saudi Arabia
[6]Department of Computer Science, College of Computer Engineering and Sciences in Al-Kharj, Prince Sattam bin Abdulaziz University, Al-Kharj, Saudi Arabia
[7]Civil Engineering Department, College of Engineering, Imam Mohammad Ibn Saud Islamic University (IMSIU), Riyadh, Saudi Arabia

*Corresponding Author: Arsalan Mahmoodzadeh. Email: arsalan@lfu.edu.krd

Received: 27 April 2026; Accepted: 09 June 2026; Published: 30 June 2026

ABSTRACT: Concrete manufacturing consumes vast quantities of natural resources and contributes significantly to environmental degradation and carbon emissions. Therefore, integrating recycled waste substances into concrete has become a crucial approach to fostering eco-friendly building practices and supporting circular economy concepts. This study investigates the potential of incorporating recycled aluminum beverage can crumbs (RABCC) as a partial replacement for natural coarse aggregates (NCA) in concrete mixtures, focusing on its impact on compressive strength (CS) and the feasibility of its application in structural concrete. A comprehensive experimental program was conducted to assess the mechanical properties of concrete with varying levels of RABCC (up to 30%) and its interaction with other mix parameters, including water-to-cement ratio (w/c), superplasticizer content (SPC), silica fume content (SFC), and curing time (CT), fine aggregate content (FAC), coarse aggregate content (CAC), fly-ash content (FA–C). The experimental findings revealed that low levels of RABCC incorporation (≤5%) led to minimal reductions in CS, with strengths comparable to those of the reference mix. However, at higher replacement levels, significant reductions in CS were observed, with the CS decreasing by up to 29.8% at 20% RABCC. To predict CS across different RABCC contents, a series of machine learning models, including kernel-based methods, ensemble tree models, gradient boosting techniques, and neural networks, were developed and validated using both hold-out and 5-fold cross-validation. The Gaussian process regression (GPR) model demonstrated the best performance, achieving an R^2 of 0.88 and an root mean squared error (RMSE) of 3.33 MPa in hold-out testing, and an R^2 of 0.89–0.94 and an RMSE of 2.37–3.10 MPa in 5-fold cross-validation, confirming its robustness in predicting CS. Additionally, SHapley Additive exPlanations (SHAP) analysis identified the w/c ratio and RABCC content (RABCC–C) as the most influential factors on CS, with RABCC–C exhibiting a moderately negative correlation. This study demonstrated the potential of RABCC as an eco-friendly, sustainable alternative to conventional aggregates in concrete, offering a viable pathway to reduce aluminum waste without significantly compromising the material's mechanical performance. The results also underscored the importance of optimizing RABCC content to balance sustainability goals with structural performance.

KEYWORDS: Recycled aluminum beverage cans crumb; concrete; compressive strength; sustainability; machine learning

1 Introduction

The building sector ranks among the foremost consumers of natural resources worldwide and simultaneously one of the most significant contributors to greenhouse gas emissions, energy consumption, and construction and demolition waste generation. Traditional concrete manufacturing demands large amounts of cement, natural sand, and coarse aggregates, leading to severe depletion of raw materials and significant environmental challenges. As a result, there has been a surge in global research efforts to develop sustainable concrete solutions by integrating recycled materials, industrial by-products, and waste-based additives into cementitious composites. The key goals of these approaches include lessening reliance on virgin resources, reducing landfill waste, cutting embodied carbon emissions, and fostering circular economy principles within the construction industry [1–5].

A variety of waste materials have shown notable promise as partial substitutes for cement, fine aggregates, coarse aggregates, or reinforcement elements in concrete blends. Notably, fly ash, silica fume, slag, crumb rubber, recycled concrete aggregates, construction and demolition debris, waste fibers, aluminum residues, and polymer wastes have garnered considerable scientific interest due to their ecological and technical merits. Dizon et al. [1] thoroughly evaluated sustainable concrete mixes incorporating laterite aggregates, fly ash, sisal fibers, and superplasticizers, demonstrating that well-optimized combinations of waste-derived components can simultaneously enhance compressive strength (CS), tensile strength, flexural performance, and cost-effectiveness while reducing environmental footprints. Similarly, Budziński et al. [4] validated that recycled aggregates incorporated in cement-bound granular composites can boost mechanical properties and promote waste valorization alongside circular economy practices in infrastructure projects.

The ecological importance of recycled aggregate concrete (RAC) has been extensively explored through life-cycle assessments and sustainability evaluations. Marinković and Carević [2] showed that RAC substantially reduces global warming potential and environmental impacts compared to standard natural-aggregate concrete, especially when CO_2 absorption and recycling methods are adequately integrated. Similarly, Kisku et al. [3] critically analyzed over 200 studies on RAC and found that, although recycled aggregates may slightly compromise durability and mechanical properties compared with traditional concrete, the use of suitable admixtures and optimized mixing techniques can effectively mitigate these limitations. Senaratne et al. [5] further highlighted that broader adoption of RAC in structural applications requires overcoming technical, industrial, and regulatory hurdles to achieve sustainable construction goals fully.

Lately, there has been a growing focus on using aluminum-based waste in cementitious materials due to aluminum's remarkable recyclability, corrosion resistance, lightweight properties, and the significant volume of global waste. Al-Alimi et al. [6] provided an extensive review of eco-friendly aluminum recycling methods, showing that secondary aluminum recycling delivers considerable environmental, energy, and economic benefits compared to primary aluminum production. In the realm of concrete engineering, numerous researchers have investigated the incorporation of aluminum waste in various forms, such as aluminum fibers, aggregates, composite panel waste, and dross. Paktiawal and Alam [7] noted that aluminum composite panel waste typically decreased workability and CS at higher substitution rates. Similarly, Khai and Ha [8] found reductions in CS and elastic modulus when recycled aluminum can fibers were incorporated into concrete. However, the material showed promise for lightweight, non-structural applications. Othman and Herki [9] observed that aluminum waste aggregates increased porosity and reduced strength, whereas hybrid mixes with recycled steel fibers enhanced ductility and freeze–thaw resistance. Conversely,

Hafez and Abd-Al Ftah [10] demonstrated that carefully calibrated amounts of waste aluminum fibers could enhance toughness and resistance to brittleness in high-strength concrete. Additionally, Mailar et al. [11] reported that recycled aluminum dross can enhance the durability and hot-weather resilience of concrete at optimal replacement levels, while Amanullayeva et al. [12] developed lightweight, thermally resistant concrete composites using various aluminum wastes.

Despite the extensive research on recycled-material concrete, a notable knowledge gap persists regarding the use of recycled aluminum as a partial replacement in concrete. Prior work on aluminum waste concrete has mainly focused on fibers, dross, or coarse waste particles, while the mechanical characteristics and predictive modeling of concrete incorporating recycled aluminum beverage can crumb (RABCC) remain largely unexamined. The environmental and economic importance of aluminum recycling has been emerging, based on emission reductions, waste disposal, the reclamation of scarce resources, and, most importantly, power savings [13]. The portion of worldwide aluminum production from secondary sources, essentially the recycling of aluminum scrap metal, is already at 30% [14]. As the demand for sustainable packaging increases worldwide, aluminum, notably in beverage cans, plays a crucial role in the shift toward a circular economy [15]. According to projections from the International Aluminum Institute (IAI) for 2024, global aluminum beverage can use is expected to grow from around 420 billion units in 2020 to nearly 630 billion by 2030, underscoring the importance of aluminum in sustainable materials management [16]. Moreover, data from the U.S. Geological Survey (2024) indicate steady expansion in worldwide aluminum mining and scrap recycling, with secondary aluminum accounting for nearly one-third of global output [17].

Aluminum beverage cans account for around 10% of total aluminum consumption by end-use. Consumption of beer and soda in aluminum cans reaches 1800 billion cans per year. While the recycling rate of aluminum cans in Germany was 99% in 2019, that in Cyprus was less than 30% due to limited Aluminum recycling facilities [16]. The beverage cans that are not recycled go to a landfill. These litter-induced negative impacts range from the absolute waste of material value, a financial roller-coaster for local councils, and the annual deaths of possibly three million small mammals [18]. The environmental pressures posed by littered cans, given their difficulty of recycling with large-scale technology, drive the aluminum industry to evolve to a point where it continues to grow while optimizing its environmental performance [16].

The integration of recycled aluminum beverage can crumb (RABCC) into the construction sector represents a pivotal opportunity not only to reform waste management but also to substantially reduce environmental impacts. Concrete, one of the most widely used materials in construction, offers significant potential for sustainability through innovation [19–22]. By substituting a fraction of the traditional coarse aggregates with RABCC, the construction industry can significantly increase the recycling rate of aluminum beverage cans worldwide. The allure of using RABCC lies in its ease of use and availability. Unlike standard recycling methods that require extensive factory setups and substantial financial commitments, adopting RABCC in concrete manufacturing requires few industrial inputs. This not only renders it a budget-friendly option but also enables local construction sectors to embrace green practices effortlessly.

Furthermore, RABCC, as an eco-conscious alternative in concrete mixtures, revolutionizes efforts to reduce carbon emissions in the construction industry. The ecological advantages are twofold: it redirects aluminum waste from dumpsites, thereby reducing pollution, and lowers dependence on conventional raw materials, thereby aiding the preservation of natural assets. This groundbreaking method can reshape waste management in construction, providing an efficient and scalable solution to address the escalating global issues of waste and resource depletion. However, integrating RABCC into concrete requires a thorough and systematic investigation to fully understand its impact on the material's mechanical properties. Concrete's strength, endurance, and overall functionality are vital to maintaining the safety and longevity of structures. Therefore, assessing how RABCC affects key attributes such as compressive strength (CS), tensile strength,

workability, and resistance to cracking or deterioration over time is imperative. Moreover, identifying the optimal RABCC proportion for concrete mixes is paramount. This process entails determining the optimal balance between the advantages of aluminum crumb inclusion and the required structural soundness. Excessive use of RABCC may reduce strength or durability, whereas insufficient use may fail to deliver notable environmental or economic gains. To address these challenges, an integrated experimental–computational framework can be adopted that synergistically combines controlled laboratory testing with advanced machine learning techniques.

Over the past few years, the assessment of engineering structures and the materials used in them through laboratory testing, analytical models, and numerical simulations has become a major area of study [23–27]. Machine learning has emerged as a valuable tool for predicting the CS of concrete incorporating different recycled aggregates such as silica fume, slag, and fly-ash [28], foundry sand [29], steel slag [30], brick [31], polymer [32], geopolymer [33], copper slag [34], and aluminum cans [35]. Each study in this field has introduced a machine-learning-based model as a potential approach for estimating and optimizing the CS of concrete containing recycled aggregates. Machine learning has become prevalent for predicting and optimizing the CS of concrete, including concrete with recycled aggregates. Behnood and Golafshani [29] developed ensemble machine learning models for geopolymer-recycled aggregate concrete, demonstrating that boosting algorithms such as extreme gradient boosting regression (XGBoost) and light gradient boosting machine (LightGBM) can accurately predict CS, while identifying curing age and recycled aggregate content as major influencing factors. Penido et al. [30] applied ensemble techniques to recycled brick aggregate concrete and demonstrated the outstanding performance of a stacking model (R^2 = 0.95), corroborated by feature significance and partial dependence studies, which elucidated the impact of mix ingredients.

Regarding steel slag concrete, Mai et al. [31] developed support vector regression (SVR), artificial neural networks (ANN), XGBoost, and Gaussian process regression (GPR) models using a comprehensive dataset and found that ANN yielded the best results reported in the literature. However, experimental validation revealed difficulties stemming from data variability and model generalizability. Han et al. [32] experimentally investigated recycled aggregate concrete with copper slag under elevated temperatures and identified an optimal combination of 33% recycled coarse aggregate and 20% copper slag, achieving enhanced strength with strong statistical correlations (R^2 = 0.98). Focusing on waste foundry sand, Golafshani et al. [33] utilized the M5P model tree algorithm to accurately forecast CS and other mechanical characteristics based on mix ratios and curing duration. Sahu et al. [34] employed a random forest regression (RFR) model to predict and refine the CS and the density of plastic aggregate concrete, achieving minimal prediction error and demonstrating the potential of machine learning-driven mix design optimization.

Alongside the research highlighted earlier, numerous studies have explored the use of machine learning methods to forecast the CS of concrete incorporating various recycled materials and supplementary components. Likewise, numerous studies have investigated the use of aluminum-based waste in cementitious composites from both experimental and sustainability viewpoints [9–12,35]. However, the literature on RABCC used specifically as an aggregate substitute in concrete remains relatively sparse, particularly when integrating experimental data with advanced machine learning and explainable artificial intelligence frameworks.

Research to date on aluminum waste in concrete has largely centered on separate experimental trials, durability assessments, fiber-reinforcement applications, or traditional statistical methodologies. Conversely, extensive data-driven studies that combine broad experimental datasets with sophisticated machine-learning predictions, rigorous cross-validation methods, and interpretable artificial intelligence approaches for RABCC concrete remain limited. Consequently, this study intends to advance this growing field by establishing a cohesive experimental and computational framework to assess and forecast the CS

performance of concrete containing RABCC. To fulfill this goal, a comprehensive experimental database was created through meticulous mix design, specimen fabrication, curing, and CS measurement across various curing times. Crucial mixture parameters, including the RABCC replacement fraction, particle size, water-to-cement ratio (w/c), binder composition, and curing period, were systematically varied within realistic engineering limits to capture both linear and nonlinear effects on the evolution of strength. Leveraging this experimentally derived dataset, multiple advanced machine learning models were developed, trained, and validated to predict CS trends and determine optimal levels of RABCC incorporation. Extensive validation methods, such as hold-out testing and k-fold cross-validation, were applied to enhance model robustness and reduce overfitting. In addition, explainable artificial intelligence techniques, notably SHapley Additive exPlanations (SHAP), were deployed to measure the relative impact and interaction of mixture parameters on CS development. By integrating experimental investigation, machine-learning prediction, and interpretable modeling, the present study provides a comprehensive framework to improve understanding and optimize RABCC-modified concrete for sustainable construction-material applications.

2 Research Significance and Scope

The incorporation of RABCC into concrete formulations represents a revolutionary approach to waste management, environmental responsibility, and resource conservation in the construction sector. Concrete, as one of the most widely used materials in construction, offers significant potential for sustainability improvements. The investigation detailed in this paper addresses a crucial gap in understanding how RABCC can partially replace conventional aggregates in concrete blends, offering opportunities to enhance sustainability by redirecting aluminum refuse from landfills. This research is of considerable importance given the rising global demand for aluminum recycling and the growing ecological challenges related to waste disposal and carbon emissions from concrete manufacturing.

The research evaluates not only the ecological advantages of incorporating RABCC but also its effects on the mechanical properties of concrete, particularly its CS, a crucial factor in assessing the longevity and safety of concrete structures. Through a holistic strategy that integrates stringent laboratory experiments with sophisticated machine learning, the study aims to forecast the optimal proportions of RABCC integration that balance recycling advantages with concrete's structural requirements. This work also examines the intrinsic interactions among essential mix factors, including w/c ratio, superplasticizer dosage, curing duration, and RABCC proportion, to understand their roles in strength progression. Employing machine learning models further enhances the study by enabling accurate predictions and optimization, leading to more effective and environmentally friendly concrete mixture formulations. Consequently, the research provides valuable insights into the feasibility of embedding recycled components into concrete, thereby advancing both conceptual understanding and practical implementation in eco-conscious construction methodologies.

3 Methodology

3.1 Feature Selection

Before building the model, the experimental dataset underwent a thorough preprocessing routine to enhance numerical robustness and ensure uniformity across models. Initially, the dataset was inspected for missing values, duplicated records, and inconsistent entries. The completed dataset showed no instances of absent data. Continuous variables were standardized via Min-Max normalization, mapping all features to the $[0, 1]$ interval, which helped minimize scaling biases and facilitated better convergence in kernel-based and neural network models. The categorical variable representing curing time (CT) was converted via one-hot encoding to retain its nominal nature while making it suitable for machine learning techniques.

The process of choosing features relied on engineering importance, previous understanding of concrete materials, and correlation evaluations. All selected variables were retained because each parameter demonstrated direct physical relevance to CS development in RABCC concrete. No dimensionality-reduction methods were used, given the moderate size and the physically interpretable nature of the feature space.

3.2 Machine Learning Models

In this study, nine distinct machine learning algorithms were employed to predict the CS of concrete containing RABCC. The primary objective was to systematically evaluate each model's predictive capability and identify the most reliable and accurate algorithm for this application. The selected models represent a diverse set of learning paradigms, including kernel-based methods, ensemble tree models, gradient boosting techniques, and neural networks. This diversity ensures comprehensive coverage of both linear and highly nonlinear relationships inherent in concrete mixtures containing RABCC, where material heterogeneity and complex interactions among input variables play a critical role. Each algorithm was chosen for its proven performance on regression problems, robustness to overfitting, and suitability for modeling nonlinear relationships in civil engineering materials. Brief descriptions of each model and the rationale for its selection are provided below.

SVR

SVR is a robust kernel-driven regression methodology originating from support vector machines (SVMs). It operates by mapping the input data into a high-dimensional feature space and identifying an optimal hyperplane that minimizes prediction errors within a predefined tolerance margin (ε). SVR excels at capturing complex nonlinear patterns and demonstrates robust generalization. This technique was chosen for the current research due to its suitability for small to moderately sized datasets and its ability to model intricate, nonlinear relationships between mixture parameters and CS in concrete containing RABCC.

Nu-support vector regression (NuSVR)

NuSVR extends the traditional SVR by incorporating the parameter Nu (ν), which governs the ratio of support vectors and permissible margin errors. This additional flexibility enables more precise control over model complexity and error thresholds, making NuSVR particularly advantageous for datasets with noise or outliers. NuSVR was included to evaluate whether its improved parameter tuning could yield superior predictive accuracy and robustness relative to classic SVR on the concrete dataset.

GPR

GPR represents a nonparametric, probabilistic regression method that models distributions over potential functions rather than pinpointing a single fixed function. By employing kernel functions to quantify similarity between data points, GPR excels at capturing smooth, nonlinear trends and provides uncertainty quantification for predictions. It was chosen for its exceptional forecasting precision, solid theoretical basis, and ability to assess prediction uncertainty, which is particularly valuable for evaluating CS in novel and sustainable concrete materials.

RFR

RFR is a collective learning technique that combines numerous decision trees, each trained on resampled versions of the dataset. The final prediction is obtained by averaging the outputs of individual trees, which significantly diminishes variance and enhances generalization. RFR was selected for its resilience to overfitting, capacity to represent intricate interactions among variables, and proficiency in handling nonlinear relationships that often arise in concrete mix design challenges.

XGBoost

XGBoost is a highly refined gradient boosting system that builds an ensemble of decision trees, with each subsequent tree aiming to correct the mistakes of its predecessors. It employs regularization methods to reduce overfitting and is celebrated for its exceptional performance and computational speed. XGBoost was adopted for its impressive track record in regression and its ability to capture complex feature interactions while delivering remarkably accurate predictions.

Gradient boosting regression (GBR)

GBR is an ensemble technique rooted in boosting that progressively constructs decision trees by minimizing a chosen loss metric. In contrast to random forests, GBR aims to reduce bias by sequentially enhancing weak predictors. This method was selected to assess the proficiency of traditional gradient boosting in forecasting the CS of sustainable concrete and to serve as a comparative standard against more sophisticated boosting algorithms, such as XGBoost, as well as histogram-oriented techniques.

Extra tree regression (ETR)

ETR is an ensemble technique closely related to RFR, but it incorporates additional stochasticity during model construction. In contrast to RFR, which selects the best split thresholds by minimizing impurity, ETR chooses split points at random for each candidate feature while still aggregating predictions across a vast ensemble of trees. This heightened randomness reduces variance and improves generalization, especially in datasets characterized by multicollinearity and intricate feature interactions. ETR was chosen for this research to evaluate whether greater randomization might enhance robustness and predictive stability when modeling the CS of sustainable concrete, where nonlinear interactions among mixture proportions, curing conditions, and recycled aggregate content are notable. Its computational efficiency and lower sensitivity to noise make ETR a significant benchmark among tree-based ensemble models.

Decision tree regression (DTR)

DTR is a non-parametric approach that partitions the input domain into nested regions guided by decision criteria based on feature values. Even though decision trees can overfit, they offer high interpretability and can model nonlinear relationships. DTR served as a foundational model for delivering an interpretable benchmark to assess the performance of more advanced ensemble and kernel-driven methods.

ANN

ANNs draw inspiration from biological systems and consist of networks of neurons arranged in multiple layers, capable of capturing intricate, nonlinear, and complex patterns through backpropagation. ANNs are widely used in material science and concrete engineering due to their flexibility and strong approximation capabilities. The ANN technique was used to evaluate its proficiency in modeling the intricately intertwined multivariate factors influencing the CS of sustainable concrete, and to benchmark its results against those of decision-tree and kernel-driven models.

The ANN framework was constructed as a multilayered perceptron (MLP) regression model comprising an input layer, three hidden layers, and a single output neuron corresponding to CS prediction. The best hidden-layer configuration discovered via Optuna optimization consisted of three hidden layers, each containing 32 neurons [(32, 32, 32)]. The rectified linear unit (ReLU) activation function was applied to the hidden layers due to its efficient computation and ability to mitigate vanishing gradient problems. The output layer employed a linear activation function suitable for continuous regression tasks. Model training was conducted using the Adam optimizer with adaptive learning-rate scheduling. The batch size and training epochs were fine-tuned during hyperparameter optimization, yielding an ideal batch size of 8 and 100 epochs. Additionally, early stopping mechanisms were implemented to minimize overfitting and enhance the model's generalization abilities.

3.3 Computational Environment and Software Implementation

The analysis for all machine learning tasks was performed in Python (Version 3.11) using the Jupyter Notebook environment. The computational workflow was performed using Scikit-learn, XGBoost, Optuna, NumPy, Pandas, Matplotlib, Seaborn, and SHAP libraries. Model training and tuning were performed on a workstation with an Intel Core i7 CPU, 32 GB of RAM, and Windows 11. To ensure reproducibility of computations, a consistent random seed of 42 was used during dataset partitioning, cross-validation, hyperparameter tuning, and model initialization whenever randomness was involved.

3.4 Hyperparameter Optimization

To ensure exceptional results, the hyperparameters of machine learning models were meticulously refined using the Optuna optimization framework based on the Tree-structured Parzen Estimator (TPE) algorithm. Optuna employs an efficient search technique founded on tree-structured Parzen estimators (TPE) along with other sophisticated algorithms, enabling it to navigate the hyperparameter space and discover the top-performing configurations. This method has demonstrated its efficacy in significantly boosting model accuracy by systematically tuning hyperparameters, including learning rate, kernel functions, the number of estimators, and regularization parameters. Every model experienced an exhaustive hyperparameter optimization routine.

A set of 200 separate tuning attempts was executed to systematically explore the hyperparameter search space and identify the optimal parameter combination that minimized prediction error on the validation dataset. Throughout the tuning process, the 5-fold cross-validation technique was used to improve generalization performance and reduce the likelihood of overfitting. The goal function aimed to minimize the root-mean-square error (RMSE) while maximizing the coefficient of determination (R^2). The specific parameters and their corresponding search ranges are outlined in Table 1.

Table 1: Optimized hyperparameters and their search ranges for each model using the Optuna method.

Model	Hyperparameter	Optimized Value/Type	Search Range
SVR	C	80	1–1000
	epsilon	0.01	0.001–1
	kernel	rbf	{rbf, poly, sigmoid}
	gamma	0.1	1e−4–1
NuSVR	C	200	0.1–1000
	nu	0.4	0.01–1
	kernel	rbf	{rbf, poly, sigmoid}
	gamma	0.1	1e−4–1
	tol	0.003	–
	shrinking	True	{True, False}
GPR	RBF length-scale	1	0–5
	Alpha	0.2	1e−12–1
	kernel	RBF	{RBF, WhiteKernel}
	random_state	42	–
XGBoost	colsample_bytree	Best from GridSearchCV	0.5–0.9
	n_estimators	Best from GridSearchCV	{100, 200}
	max_depth	Best from GridSearchCV	{10, 15, 20, 25}

(Continued)

Table 1 (continued)

Model	Hyperparameter	Optimized Value/Type	Search Range
	objective	reg:squarederror	–
	cv	5-fold	–
GBR	loss	squared_error	{squared_error, absolute_error, huber}
	learning_rate	0.1	0.01–0.8
	max_leaf_nodes	20	10–50
	max_depth	None	2–None
	min_samples_leaf	15	1–50
	validation_fraction	0.2	0.1–0.3
	n_iter_no_change	5	1–20
	tol	1e−08	1e−10–1e−3
ETR	criterion	absolute_error	{squared_error, absolute_error}
	n_estimators	7	1–1000
	max_depth	30	5–None
	min_samples_split	2	2–20
	min_samples_leaf	1	1–10
	max_features	7	{sqrt, log2, integer}
	bootstrap	False	{True, False}
	warm_start	True	{True, False}
DTR	criterion	squared_error	{squared_error, friedman_mse, absolute_error}
	random_state	0	–
RFR	n_estimators	Best from RandomizedSearchCV	20–200
	max_features	Best from RandomizedSearchCV	{auto, sqrt}
	max_depth	Best from RandomizedSearchCV	10–110, None
	min_samples_split	Best from RandomizedSearchCV	{2, 5, 10}
	min_samples_leaf	Best from RandomizedSearchCV	{1, 2, 4}
	bootstrap	Best from RandomizedSearchCV	{True, False}
	cv	5-fold	–
ANN	batch_size	8	8–64
	epochs	100	50–150
	hidden_layer_sizes	(32, 32, 32)	{(32,32), (64,64), (32,32,32)}
	activation	relu	{relu, tanh, sigmoid}
	optimizer	adam	{adam, rmsprop, sgd}

(Continued)

Table 1 (continued)

Model	Hyperparameter	Optimized Value/Type	Search Range
	output_activation	relu	{linear, relu}
	loss	mse	{mse, mae}

4 Database

An extensive experimental database was constructed to facilitate both the statistical analysis and machine learning modeling presented in this study. Overall, 850 concrete cube specimens (150 mm × 150 mm × 150 mm) were fabricated, cured, and tested under systematically varied mix-design parameters, including various RABCC incorporation levels, w/c ratios, aggregate proportions, supplementary cementitious material contents, and curing durations. The compiled dataset served as the foundation for all machine learning training, hold-out validation, k-fold cross-validation, SHAP interpretation, and statistical analyses performed in this research.

4.1 Preparation of the Data Points and CS Testing

To guarantee that the CS outcomes were trustworthy, consistent, and statistically valid, a thoroughly organized and methodical experimental program was implemented to create a specialized database for concrete incorporating RABCC. Given that no standardized experimental database currently exists for this material system, all data used in the present study were generated exclusively through controlled laboratory experiments conducted under carefully monitored conditions.

In total, 850 concrete cube specimens (150 mm × 150 mm × 150 mm) were prepared and tested. It is important to note that these 850 specimens do not represent 850 unique mixture designs; rather, they denote the total number of specimens derived from various mixture formulations, repeated batches, replicated specimens, and varying curing durations to ensure statistical soundness and machine-learning reliability. The experimental matrix included systematic variations in the RABCC replacement ratio, w/c ratio, supplementary cementitious material content, aggregate proportions, curing time, and superplasticizer dosage. Multiple replicate specimens were tested for each mixture condition to minimize experimental uncertainty and improve the consistency of the resulting database. The complete mix-design matrix, batching scheme, specimen distribution, and raw experimental dataset are provided in the Supplementary Material accompanying this manuscript to improve reproducibility and research transparency.

Across the experimental campaign, roughly 6.8 metric tons of concrete, equating to about 2.87 m^3 of material, were produced. This substantial production volume ensured sufficient volumetric consistency, typical batching conditions, and dependable evaluation of mixture variability during all testing phases. A schematic representation of the experimental methodology, database preparation procedure, specimen distribution, and analytical workflow is presented in Fig. 1.

At the outset, a reference control mixture was designed to serve as the baseline for all RABCC-modified concrete mixtures. The control mix included approximately 350 kg/m^3 of total cementitious materials with a target w/c of 0.45, chosen to ensure a harmonious blend of workability, mechanical performance, and mixture stability. Natural fine and coarse aggregates were measured in accordance with standard grading requirements. RABCC was then introduced as a partial replacement material, and the replacement ratios were carefully adjusted over a broad range to reflect both beneficial and negative effects on CS development. At each replacement level, the aggregate quantities were recalculated to preserve consistent total aggregate volume and overall mixture homogeneity.

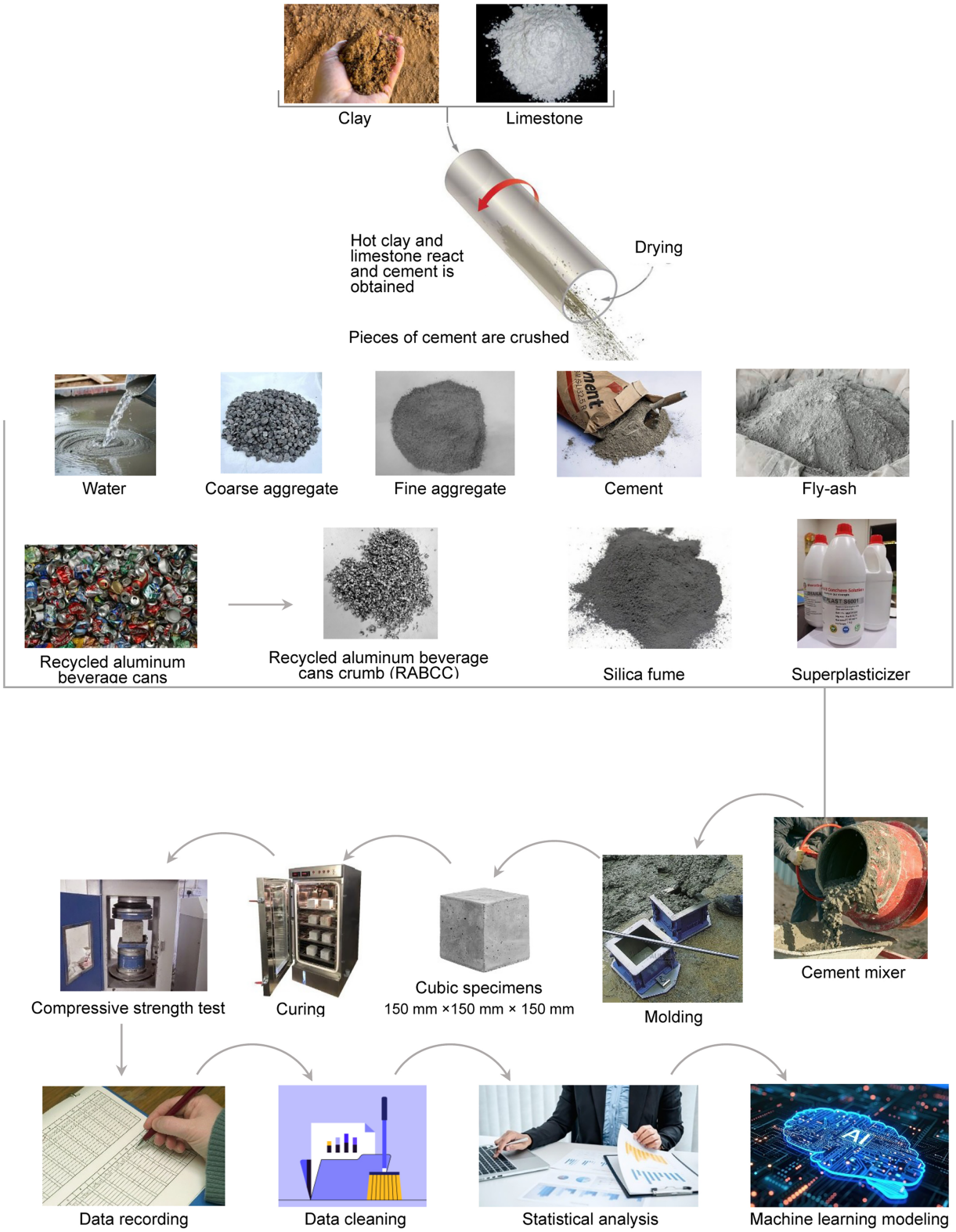

Figure 1: Schematic overview of the database preparation, experimental procedures, and analytical workflow.

The physical characteristics of the RABCC are outlined in Table 2. The determined specific gravity of 2.68 was notably lower than that of conventional natural coarse aggregate, highlighting the lightweight nature of aluminum-based particles. The comparatively low loose and compacted bulk densities further demonstrate the reduced unit weight and packing efficiency of RABCC relative to mineral aggregates. The water absorption capacity of the RABCC was only 0.42%, which is substantially lower than that typically observed for conventional porous aggregates. This behavior is attributed to the dense metallic structure and smooth surface characteristics of aluminum particles. Although the low absorption limits internal moisture uptake, the smooth metallic surface reduces mechanical interlocking. It weakens the interfacial transition zone (ITZ) between the RABCC particles and the surrounding cement paste. However, since no direct microstructural characterization techniques, such as scanning electron microscopy (SEM), energy-dispersive spectroscopy (EDS), X-ray diffraction (XRD), or Fourier-transform infrared spectroscopy (FTIR), were implemented in this paper, any interpretations regarding the behavior of the ITZ or bonding characteristics must be considered indirect and rely primarily on macroscopic mechanical observations and available literature. Sieve analysis confirmed that the particle size distribution ranged from 0.5 to 4.0 mm, with a mean particle size of 2.11 mm, consistent with the chosen aggregate replacement strategy for the concrete mix design. The RABCC particles exhibited irregular angular morphology and smooth metallic surfaces, traits that significantly influenced workability, packing density, porosity development, and CS behavior at elevated replacement levels. Accordingly, minor adjustments to mixing water and superplasticizer content (SPC) were implemented while maintaining the target effective water content.

Table 2: Physical properties of RABCC.

Property	Measured Value
Specific gravity	2.68
Bulk density (loose condition)	785 kg/m^3
Bulk density (compacted condition)	842 kg/m^3
Water absorption capacity	0.42%
Particle size range	0.5–4.0 mm
Mean particle size	2.11 mm
Maximum particle size	4.0 mm
Surface texture	Smooth metallic surface
Particle morphology	Irregular angular crumb particles
Color and appearance	Silver-gray metallic particles

The preparation of concrete involved using a laboratory-scale forced-action mixer with a batch size of approximately 50 kg, yielding six cube specimens per batch. All constituents were weighed using calibrated precision scales before mixing. Dry materials, including cement, supplementary cementitious materials (such as fly ash and silica fume), fine aggregate, coarse aggregate, and RABCC, were initially combined for 30–60 s to guarantee uniform distribution. Next, around half of the mixing water, pre-blended with the superplasticizer, was introduced, followed by the slow addition of the remaining water. The total mixing duration ranged from 2 to 4 min, depending on the mixture composition and observed workability. The consistency of fresh concrete was monitored for each batch, and all relevant parameters were recorded to ensure batch-to-batch repeatability.

The casting process was performed in accordance with established protocols to minimize inconsistencies. Cube molds were cleaned, assembled, and coated with a thin layer of release oil. Fresh concrete

was placed into the molds in two layers, each compacted using a vibrating table or tamping rod to eliminate entrapped air without inducing segregation. The visible surfaces were leveled and finished, and each specimen was marked with a unique identification code indicating RABCC content, binder composition, w/c ratio, aggregate proportions, CT, and SPC. The specimens were covered with plastic sheets and stored at laboratory conditions (20°C–25°C) for 24 ± 2 h to prevent moisture loss. After demolding, the specimens were transferred to curing tanks containing saturated limewater maintained at 20°C ± 2°C, while selected batches were cured in humidity-controlled chambers with relative humidity exceeding 95%. Specimens were cured until designated testing ages of 7, 14, 28, and 56 days, enabling the assessment of both early-age and long-term CS development.

A calibrated hydraulic press was used to conduct CS testing in accordance with BS EN 12390-3. Before starting the test, the cube's dimensions were carefully measured to ascertain the exact cross-sectional area. The load was applied concentrically at a regulated rate of 0.6 ± 0.2 $MPa \cdot s^{-1}$ until the specimen failed. The maximum load sustained was recorded, and CS was calculated as the peak load divided by the cross-sectional area. Visual inspection of failure modes, such as cracking patterns and crushing characteristics, was conducted and documented for quality assurance. All gathered experimental data were systematically entered into a digital repository, ensuring full traceability of mix compositions, curing conditions, and measured strengths. For each formulation and curing duration, summary statistics (including average compressive strength, standard deviation, and coefficient of variation) were calculated. This meticulously assembled, internally consistent experimental dataset served as the basis for the ensuing statistical analyses, machine learning models, and interpretable evaluations described in the subsequent sections.

4.2 Distribution Analysis and Identification of Extreme Data Points

Box plots in Fig. 2 illustrate the distributional characteristics of the experimental database and were employed to detect possible outliers and boundary-condition cases within the explored parameter space. These diagrams provide insight into the central tendencies, spread, and variability of the primary mixture factors that control the evolution of CS. The RABCC content (RABCC–C) exhibits a deliberately broad distribution, mirroring the methodical investigation of aluminum crumb substitution levels required to capture its potentially nonlinear effect on CS. This broad spectrum is crucial for developing robust machine learning models capable of determining optimal limits for RABCC incorporation.

The distributions of fine aggregate content (FAC) and coarse aggregate content (CAC) are relatively symmetric, with moderate interquartile ranges, indicating uniform batching procedures and controlled aggregate ratios throughout the experimental study. Likewise, the w/c ratio shows a narrow interquartile range, indicating that workability was meticulously controlled to minimize its confounding effect on strength performance. The SPC and silica fume content (SFC) features exhibit moderate variability, indicating their role in fine-tuning rheology and refining microstructure across varied mix formulations, rather than serving as primary strength-determining factors. The maximum aggregate size (MAS) shows limited variability, implying aggregate gradation was deliberately limited to isolate the impact of RABCC addition. Conversely, fly-ash content (FA–C) exhibits a broader range, consistent with its role as a supplementary cementitious material applied at varying levels to enhance packing density and long-term strength development. Across the complete database of 850 experimental data points, 12 outliers were detected, primarily corresponding to boundary-condition mixtures and extreme replacement scenarios intentionally incorporated within the experimental design space. These data points were not viewed as errors or anomalies; instead, they embody physically significant experimental settings crucial for capturing the full nonlinear response behavior of RABCC concrete. As a result, these boundary-condition observations were deliberately retained to

strengthen the robustness, expand generalization capability, and improve predictive reliability of the machine learning models across a wider spectrum of mixture formulations.

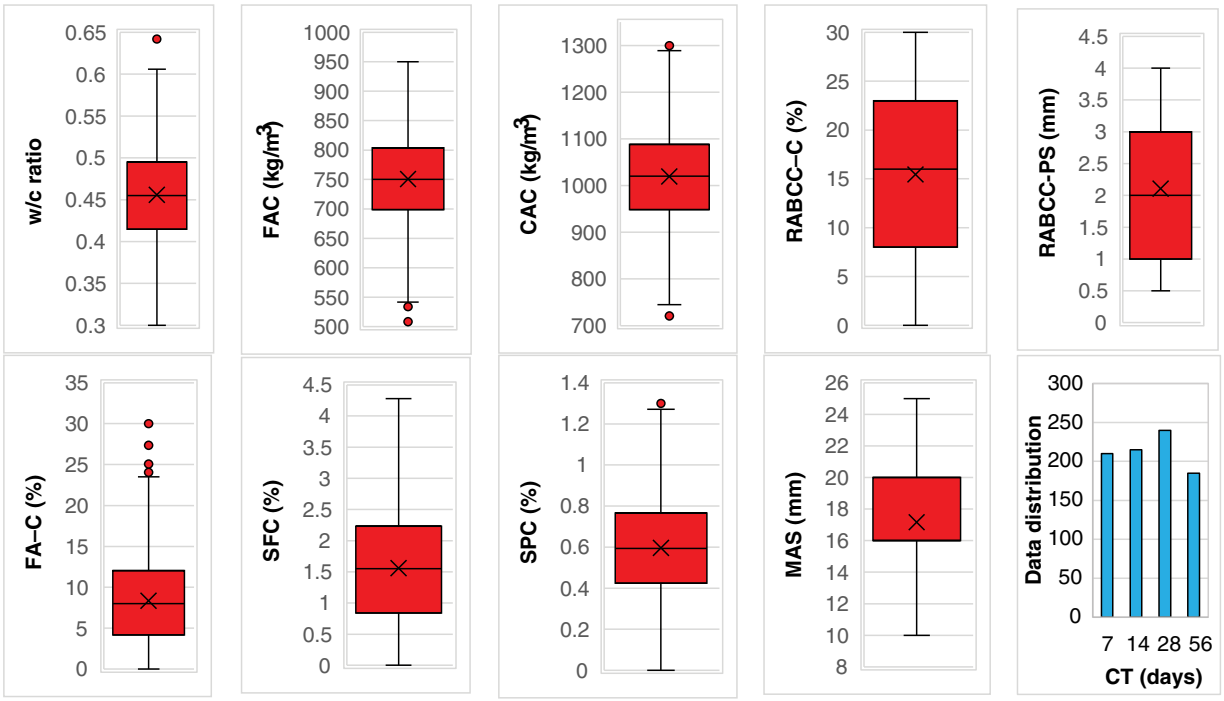

Figure 2: Box plots illustrating the distribution of numerical features and a column plot representing the categorical feature (CT).

Alongside the quantitative variables, the column plot in Fig. 2 presents the distribution of the categorical feature (CT). The dataset features four distinct curing intervals (7, 14, 28, and 56 days), deliberately chosen to capture both the initial-age and extended-strength progression of concrete incorporating RABCC. The spread of observations across these curing intervals is pretty even, ensuring that no particular age dominates the dataset. This equitable representation is vital for empowering machine learning models to capture the temporal progression of CS without favoring a specific curing period. The integration of multiple CTs deepens the database by enabling models to account for hydration kinetics and the prolonged effects of supplementary cementitious materials and aluminum crumb additives. Furthermore, the categorical classification of CT enables a clear distinction between age-dependent and mixture-dependent influences in modeling and interpretive analysis. The sufficiently large and well-distributed sample size at each curing age lays a solid foundation for examining age-specific trends, facilitating both accurate prediction and insightful SHAP-based interpretation of CT as a pivotal factor shaping CS maturation.

4.3 Statistical Analysis of the Database

Tables 3 and 4 offer an extensive statistical overview of the numerical and categorical variables constituting the experimental database developed in this study. Collectively, these tables highlight the dataset's magnitude, variety, and internal coherence, all of which are crucial for reliable statistical analysis and machine learning model development.

Table 3 presents a summary of descriptive statistics for the numerical input parameters and the target output variable (CS) based on 850 data points. The w/c ratio averages 0.46, with a relatively small standard

deviation (0.06), suggesting that workability was kept within a regulated, practical scope while still permitting sufficient variability to observe its impact on strength progression. FAC and CAC have mean values of 750.80 and 1019.37 kg/m^3, respectively, with moderate variance, indicating consistent aggregate proportions across mixtures and enabling investigation of realistic batching fluctuations.

Table 3: Statistical summary of numerical parameters.

	w/c	FAC	CAC	RABCC–C	RABCC–PS	FA–C	SFC	SPC	MAS	CS
Unit	- - -	kg/m^3	kg/m^3	%	mm	%	%	%	mm	MPa
count	850	850	850	850	850	850	850	850	850	850
mean	0.46	750.80	1019.37	15.44	2.11	8.36	1.56	0.60	17.17	35.55
std	0.06	77.23	101.17	8.85	1.21	5.45	0.96	0.24	3.64	9.73
min	0.30	508.50	720.80	0.00	0.50	0.00	0.00	0.00	10.00	4.20
25%	0.42	698.80	948.70	8.00	1.00	4.19	0.84	0.42	16.00	28.70
50%	0.46	750.15	1020.25	16.00	2.00	8.01	1.55	0.59	16.00	35.25
75%	0.50	803.88	1087.95	23.00	3.00	12.05	2.23	0.76	20.00	42.40
max	0.64	950.10	1299.90	30.00	4.00	30.00	4.28	1.30	25.00	62.20

Note: w/c: water-to-cement ratio; FAC: fine aggregate content; RABCC–C: recycled aluminum beverage cans crumb content; RABCC–PS: particle size of RABCC; FA–C: fly-ash content; SFC: silica fume content; SPC: superplasticizer content; MAS: maximum aggregate size; CS: compressive strength.

Table 4: Statistical summary of the categorical parameter (CT).

Parameter	State	Percentage of Data Points (%)	One-Hot Encoding
CT	7 days	6	10000
	14 days	9	01000
	28 days	70	00100
	56 days	9	00010
	90 days	6	00001

Note: CT: curing time.

The RABCC–C ranges from 0% to 30%, with a mean of 15.44% and a standard deviation of 8.85%, confirming that the experimental program intentionally covered a wide range of replacements. This broad range is crucial for identifying both optimal and critical thresholds for incorporating aluminum crumb. Similarly, the RABCC–PS ranges from 0.5 to 4.0 mm, with a median of 2.11 mm, ensuring that the effects of aluminum crumb gradation on CS are adequately captured.

Supplementary cementitious materials (FA–C and SFC) exhibit mean values of 8.36% and 1.56%, respectively, with distributions extending from zero to relatively high replacement levels. This variability enables the assessment of synergistic or antagonistic interactions between RABCC and pozzolanic materials. The SPC shows a narrow distribution (mean = 0.60%, standard deviation = 0.24%), indicating that chemical admixture dosage was carefully adjusted to control workability rather than dominate strength behavior. The MAS ranges from 10.00 to 25.00 mm, with a mean of 17.17 mm, which is typical of structural concrete gradations.

The target variable (CS) reveals an extensive and practical range, spanning from 4.22 to 62.20 MPa, with a mean of 35.55 MPa. This substantial spread confirms that the dataset encompasses low-, medium-, and high-strength concretes, thereby enhancing the generalizability and predictive capability of the machine learning models developed in this study.

Table 4 presents a statistical summary of the categorical parameter (CT), a critical factor governing hydration kinetics and the evolution of strength. The dataset includes five discrete curing ages (7, 14, 28, 56, and 90 days) representing approximately 6%, 9%, 70%, 9%, and 6% of the total data points, respectively. To integrate this categorical factor into the machine learning system, the CT variable was one-hot encoded. This encoding strategy preserves the non-ordinal nature of CT categories and prevents the models from incorrectly interpreting curing durations as linearly related numerical values. Each curing scenario was thus encoded as a distinct binary vector, ensuring greater clarity, numerical suitability, and prediction accuracy across the machine learning models developed.

The Pearson correlation matrix shown in Fig. 3 displays the linear connections between the main numerical variables and the target variable (CS). The matrix offers an insight into the extent and directionality of linear relationships among the examined parameters. The w/c ratio shows the strongest association with CS, with a moderate inverse correlation (−0.59). This finding aligns perfectly with established concrete technology concepts, in which an elevated w/c ratio typically reduces CS due to increased capillary porosity and weakening of the cementitious matrix. The relatively strong value of this correlation underscores the dominant effect of the w/c ratio on strength progression in the studied dataset.

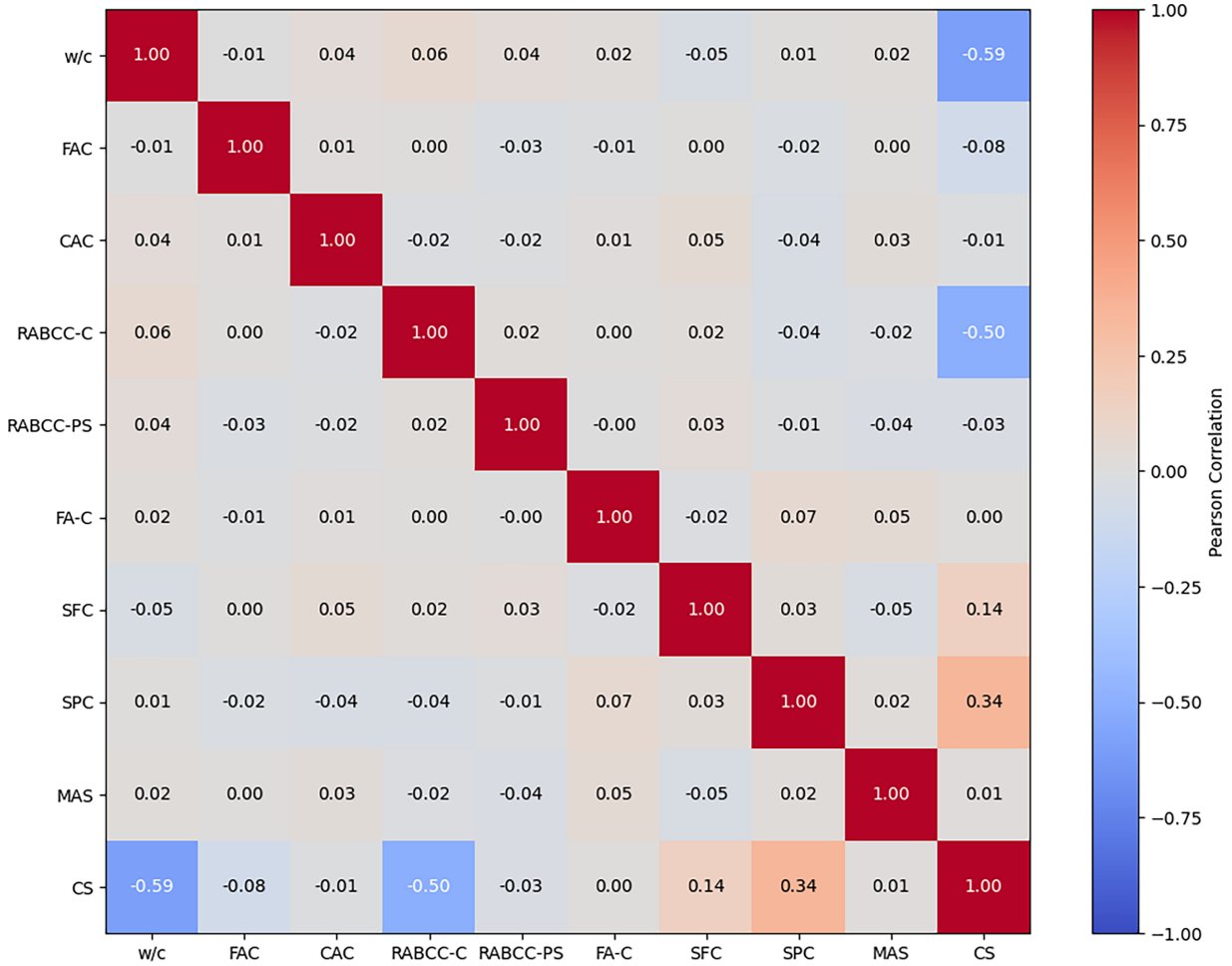

Figure 3: Pearson correlation matrix of numerical parameters.

The RABCC–C exhibits a moderate negative correlation with CS (−0.50), suggesting that higher levels of aluminum crumb substitution generally lead to decreases in CS. This pattern aligns with the observed experimental strength behavior and may be linked to the reduced stiffness and altered physical properties of recycled aluminum particles compared to traditional aggregates.

The SPC shows a moderate positive relationship with CS (0.34), suggesting that enhanced flowability and particle separation may improve compaction and strength gain. Similarly, SPC exhibits a moderate positive correlation with RABCC–C (0.34), indicating that mixtures with higher RABCC levels generally require more superplasticizer to ensure adequate fresh-state behavior.

Conversely, several other factors showed only minimal or insignificant linear connections with CS. For instance, FAC and CAC had correlation coefficients of merely 0.02 and 0.04, respectively, whereas the link between RABCC–C and the w/c ratio stood at only 0.06. These figures are statistically and practically meaningless and shouldn't be regarded as significant linear associations. Likewise, SFC, MAS, and FA–C demonstrated relatively weak linear associations with CS within the investigated experimental range, suggesting that their direct linear influence on CS was comparatively limited in the present dataset.

Fig. 4 shows the mean SHAP values, which indicate the average impact of each feature on the model's output magnitude. The SHAP evaluation, conducted with a CatBoost model, measures each feature's contribution to the outcome. The w/c ratio stands out as the most crucial factor, with a mean SHAP value substantially higher than the others, underscoring its dominant influence on the CS forecast. This reinforces the well-established understanding that the w/c ratio is fundamental to concrete's mechanical behavior, especially regarding strength development.

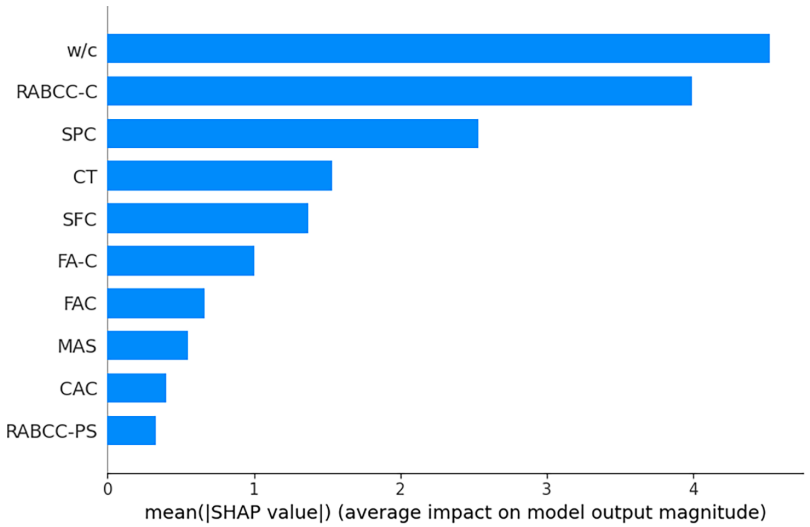

Figure 4: The importance of numerical features via SHAP (CatBoost model).

RABCC–C ranks second in significance, indicating that the integration of aluminum crumbs is a pivotal factor influencing strength. While the negative correlation between RABCC–C and CS in the Pearson matrix implies diminishing strength at higher content, this analysis shows its significant influence on model output, highlighting its potential to impact strength predictions. SPC is another key attribute, as anticipated, due to its function in improving the workability and uniformity of the mixture. Its notably elevated SHAP value indicates that the model considers it a vital factor, likely because of its direct influence on the mix's flow characteristics and compaction. CT is also considered a fairly significant factor. This is consistent with the known role of CT in concrete strength development, particularly in long-term hydration and the effects of

supplementary cementitious materials such as RABCC and fly ash. The capability to monitor age-related strength patterns is essential for a precise model. The contribution of silica fume is noteworthy, though less pronounced than w/c or RABCC–C. This aligns with expectations that SFC improves concrete's CS over time, but with a milder effect compared to other mix components. Factors such as FAC, MAS, FA-C, and CAC exhibit reduced importance, mirroring the conclusions of the correlation study. These variables may exert more localized impacts depending on the mixture details, but play a lesser role in steering the overall compressive strength forecasts.

Fig. 5 illustrates the distance correlation coefficients, which reflect the intensity of the association between each variable and CS. These coefficients offer a deeper insight into the dependency, particularly for nonlinear connections. The w/c ratio and RABCC–C exhibit the highest distance correlation values with CS (0.554 and 0.476, respectively), confirming their crucial roles in influencing CS. This aligns with both the Pearson correlation matrix and the SHAP analysis, suggesting that these features are the most influential. SPC also demonstrates a moderate correlation (0.308), underscoring its role in modulating workability and compaction, which subsequently influence strength development. The other variables, including SFC, CT, FAC, MAS, FA-C, RABCC–PS, and CAC, exhibit lower distance-correlation values, underscoring their lesser roles in influencing CS. Although relevant, they exert less influence than primary factors such as w/c ratio and RABCC–C.

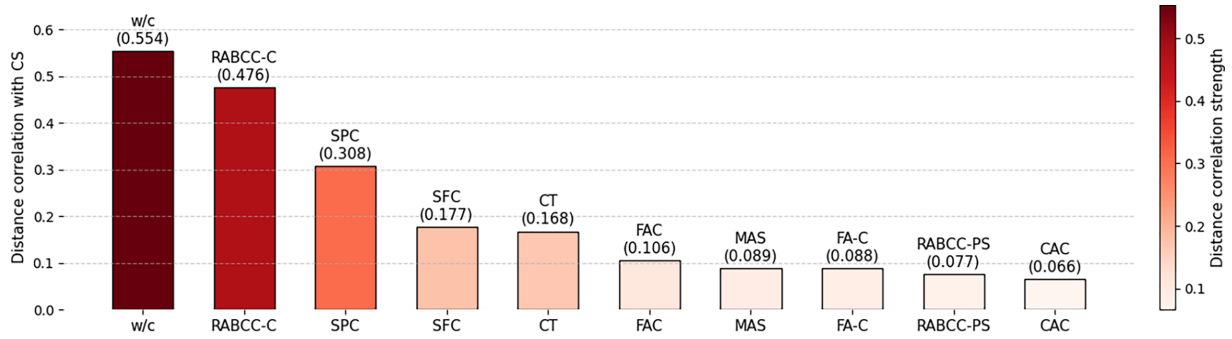

Figure 5: Distance correlation scores with CS.

Integrating Pearson correlation, distance correlation, and SHAP analyses provides a comprehensive perspective on the features that impact CS, enabling enhanced mix design optimization for sustainable concrete production using RABCC. The dataset's robustness, as evidenced by these analyses, guarantees that the machine learning models developed in this study achieve high accuracy and interpretability in predicting CS.

5 Results Analysis and Comparison

5.1 Experimental Investigations

To clearly demonstrate the impact of RABCC integration on the CS of concrete within a controlled baseline environment, 10 representative mixtures were selected from the broader experimental database comprising 850 concrete specimens. Standard features were maintained for all mixes, with fixed parameters summarized in Table 5, including w/c = 0.45, FAC = 780 kg/m^3, MAS = 19 mm, SPC = 1.0%, and CT = 28 days. By keeping these constants constant, with the only test variable the incorporation of RABCC, the program was specifically designed to establish the effects of incorporating RABCC on the CS. The variable factor across the mixtures was the replacement level of natural coarse aggregate (NCA) by RABCC, as detailed in Table 5. The RABCC-C was increased incrementally from 0% (in the absence of RABCC) in the control

mix M1 to 30% in mix M10, to include aluminum crumb content representing low, moderate, and relatively high degrees in the mix. This systematic variation, therefore, allowed a comparison between gradual changes in CS behavior and those of the control mix.

Table 5: Constant parameters used for all mixes.

Parameter	Constant Value
w/c	0.45
FAC	780 kg/m^3
RABCC–PS	3 mm
FA–C	0
SFC	0
SPC	1.0%
MAS	19 mm
CT	28 days

Note: w/c: water-to-cement ratio; FAC: fine aggregate content; RABCC–C: recycled aluminum beverage cans crumb content; FA–C: fly-ash content; SFC: silica fume content; SPC: superplasticizer content; MAS: maximum aggregate size; CT: curing time.

The results from CS tests are tabulated in Table 6 and presented graphically in Fig. 6. As presented in Fig. 6, the CS of control concrete (RABCC–C = 0) reached 42.1 MPa. Inclusion of small amounts of RABCC (1%–2%) leads only to small reductions in strength, by 1.2% and 2.4%, respectively. Small changes such as this could mean that very limited replacement levels of RABCC can be accommodated without loss of mechanical properties, because there is still minimal disruption to the aggregates' skeleton and to the load-transfer mechanism. With high RABCC replacement rates, there was a gradual, more pronounced reduction in CS. There was a fall in CS of approximately 4.8%–7.6%, with RABCC inclusion increasing from 3% to 5%, suggesting a possible adverse effect. The onset of these strength reductions can be linked not only to the smooth surface texture of RABCC and its lower stiffness relative to natural aggregates, but also to chemical and physical interactions between metallic aluminum particles and the highly alkaline cement pore solution. In cement-based systems, the alkaline conditions created by calcium hydroxide and alkali hydroxides can promote the corrosion-like reaction of metallic aluminum, resulting in the formation of hydrogen gas (H_2). The release of hydrogen gas within the fresh cement matrix can form trapped voids, microcavities, and localized pore channels, thereby increasing internal porosity and disrupting the continuity of the cementitious structure. This process reduces the density and soundness of hardened concrete and weakens the ITZ between aluminum particles and the adjacent cement paste.

At higher replacement levels (8%–12%), CS deterioration was clearly noticeable. Further reductions were observed, ranging from 13.1% to 17.9%. The influence is evident in Fig. 6 as evidenced by the downward trajectory of the 28-day CS curve and the increasingly negative CS change bars. It seems that, with respect to sufficient RABCC–NCA replacement levels, increasing porosity, reducing interfacial adhesion between reverted cement aggregates, and stress concentrations around metallic inclusions may govern the mechanical response mechanism. The strength decrease was substantial at replacement levels above 19% RABCC. The CS thus experienced reductions of 20.9%, 26.2%, and 29.8% at RABCC ratios of 19%, 23%, and 30%, respectively. The results confirm that excessive use of RABCC doesn't align with the CS and would render the mixes unsuitable for structural work unless otherwise altered or supplemented.

Table 6: Impact of increasing RABCC incorporation on the 28-day CS.

Mix ID	Coarse Aggregate Replacement	28-Days CS (MPa)	CS Change (%)
M1	100% NCA	42.1 (control)	0
M2	1% RABCC + 99% NCA	41.5	−1.2
M3	2% RABCC + 98% NCA	41.0	−2.4
M4	3% RABCC + 97% NCA	40.2	−4.8
M5	5% RABCC + 95% NCA	38.7	−7.6
M6	8% RABCC + 92% NCA	36.5	−13.1
M7	12% RABCC + 88% NCA	34.5	−17.9
M8	19% RABCC + 81% NCA	33.2	−20.9
M9	23% RABCC + 77% NCA	31.1	−26.2
M10	30% RABCC + 70% NCA	29.5	−29.8

Note: RABCC: recycled aluminum beverage cans crumb; NCA: natural coarse aggregate.

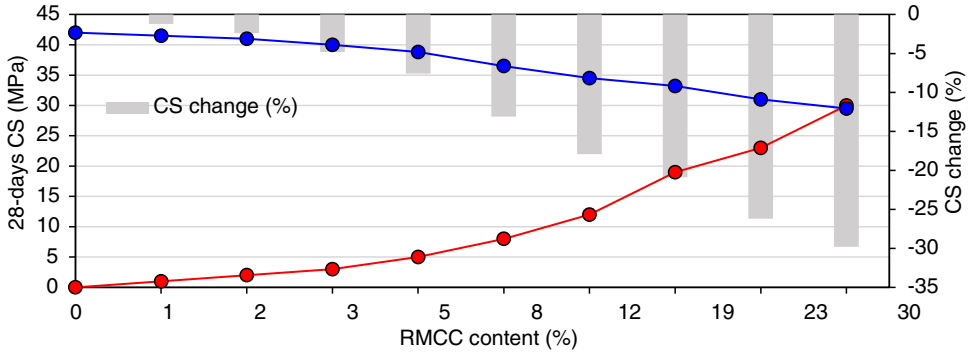

Figure 6: Change in the 28-days CS of concrete as a function of RABCC–C.

In general, Fig. 6 shows a clear, nearly monotonic relationship between increasing RABCC content and decreasing 28-day CS. The concurrent depiction of absolute strength values and percentage changes entails a broader understanding of the mechanical aftermath of RABCC incorporation. By all appearances, as far as the test outputs go, it becomes evident that low RABCC replacement ratios could be viable to some extent in sustainable concrete applications, with minor strength penalties; on the other hand, increasing replacement levels will seriously undermine mechanical properties. These findings highlight the importance of identifying an optimal RABCC content range that balances environmental benefits with structural performance requirements, a task further addressed through machine learning-based optimization in subsequent sections.

Drawing from the experimental results and the noted CS patterns, a series of pragmatic engineering guidelines can be devised for the integration of RABCC into concrete manufacturing. Although increasing RABCC content generally led to progressive reductions in CS, the material still demonstrates considerable potential as a sustainable alternative aggregate for selected concrete applications. The engineering importance of RABCC goes beyond just strength metrics and encompasses various key environmental and functional benefits, including lowering the use of natural coarse aggregates, diverting aluminum waste from landfills, minimizing the environmental impact linked to aggregate extraction and waste management,

reducing concrete density, and promoting construction practices rooted in the circular economy. Furthermore, the lightweight metallic character of RABCC could enhance thermal insulation properties and boost suitability for lightweight and non-structural concrete systems.

For structural concrete applications, where CS, structural integrity, and durability are paramount design criteria, the use of RABCC should preferably be limited to relatively low substitution rates, typically around 2% to 3% of NCA. Within this range, the observed reduction in 28-day CS generally remains below 5%, a margin often compatible with conventional structural design tolerances through mix optimization strategies, controlled curing conditions, and the use of appropriate additional chemical admixtures or cementitious materials. Therefore, the limited use of RABCC represents a technically feasible and environmentally sound approach to incorporating recycled aluminum waste into concrete production while maintaining acceptable mechanical performance and structural reliability.

For non-structural and semi-structural concrete applications, including pavements, curbs, blocks, partitions, and architectural or lightweight elements, higher RABCC contents may be considered. Replacement levels in the range of 5%–10% can be adopted where moderate reductions in CS (approximately 8%–19%) are acceptable and where enhanced sustainability, reduced density, or specific functional requirements are prioritized over maximum strength. However, RABCC contents exceeding 10%–12% are not recommended for general use, as the associated strength losses become pronounced. They may adversely affect durability and long-term performance unless compensated for by advanced mix design strategies, such as increased binder content or the incorporation of supplementary cementitious materials.

In general, the experimental results demonstrate that the engineering viability of RABCC concrete should not be assessed solely from the perspective of CS reduction. Rather, its use should be evaluated within a more extensive sustainability-driven framework that takes into account mechanical performance, environmental impact mitigation, waste reutilization efficiency, lightweight construction benefits, and conservation of natural resources simultaneously.

5.2 Hold-Out Cross-Validation

This section outlines the configuration for machine learning intended to predict the CS of concrete samples containing RABCC via the hold-out cross-validation technique. The experimental procedure consisted of three primary phases, commencing with training each model on Min-Max normalized input data, using an 80%:20% split. The model training curves are shown in Fig. 7, illustrating the trajectories of the mean squared error (MSE) for training and validation over 200 epochs. These graphs reveal a profound understanding of the progression toward different subject characteristics, learning proficiency, and how generalization appeared across multiple models. A consistent learning equilibrium was achieved by integrating training and testing targets or curves, which provided ample insight into underfitting and overfitting. In brief, each model was trained on the same standardized dataset and with the same hyperparameter tuning methods to ensure a fair comparison.

The curves shown in Fig. 7 provide critical insight into each model's learning dynamics, convergence behavior, generalization capability, and susceptibility to underfitting or overfitting when predicting the CS of concrete incorporating RABCC. In general, all models demonstrate a swift decline in both training and validation MSE during the early epochs, signifying effective learning of the dominant input–output relationships from the experimental database. This initial sharp drop is typical of well-posed regression problems where key variables such as the w/c ratio and RABCC—C strongly influence the response. As training advances, the learning curves progressively level off, indicating convergence toward stable solutions. Nevertheless, the speed of convergence, final error magnitudes, and the differences between training

and validation curves vary considerably across models, highlighting variations in model complexity and learning strategies.

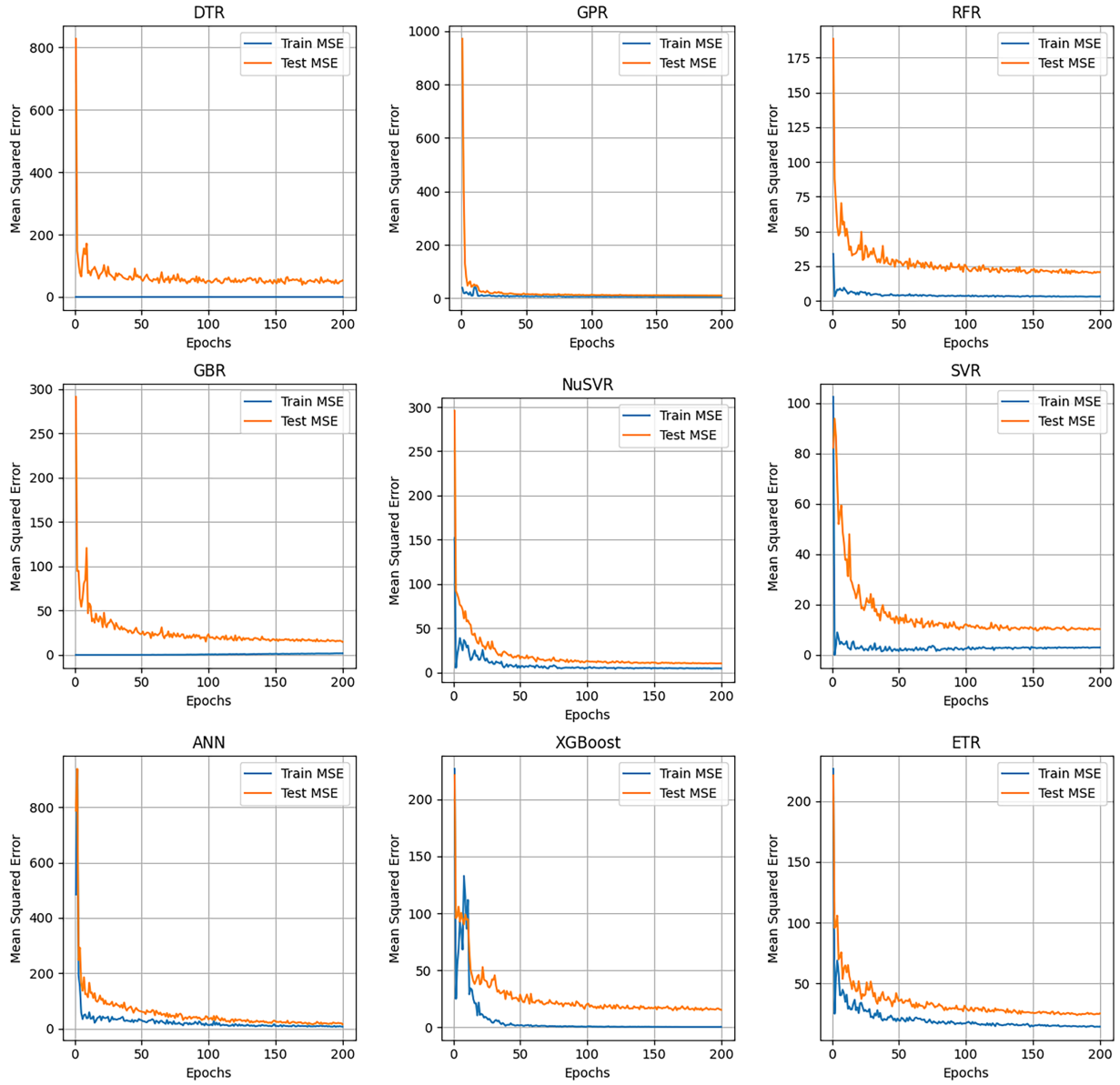

Figure 7: Learning curves of machine learning models illustrating the evolution of training and validation MSE over 200 epochs.

The DTR reveals a marked contrast between training and test MSE throughout the entire training phase. While the training error rapidly drops to very low values, the validation error remains significantly higher and exhibits noticeable fluctuations. This pattern signals the presence of overfitting, a common drawback of single decision trees, which tend to memorize the training set and struggle to generalize effectively to new data, particularly in complex, high-dimensional, and nonlinear tasks like predicting concrete strength.

The GPR exhibits remarkable convergence characteristics, with both training and validation MSE declining sharply and settling at very low, closely matched levels. The slight difference between the two

curves suggests robust generalization ability and a well-maintained equilibrium between model flexibility and regularization. This performance highlights GPR's aptitude for modeling intricate nonlinear patterns in relatively smooth experimental datasets, though it requires greater computational resources.

RFR offers a notable advancement over the single-tree method. The ensemble composition of RFR results in much lower validation MSE and a narrower gap between training and testing curves compared to DTR. Yet, a slight difference persists, indicating some degree of overfitting. Despite this, the model shows consistent convergence and strong prediction accuracy, validating the power of ensemble averaging to reduce variance while preserving robust learning potential.

GBR demonstrates a gradual, regulated decline in both training and validation MSEs, ultimately converging to relatively low error levels. The close agreement of the curves reflects effective regularization and strong generalization capabilities. In contrast to RFR, GBR seems less susceptible to overfitting, thanks to its stepwise error-correction approach that progressively enhances predictions.

Both the NuSVR and SVR models exhibit smooth convergence trends with moderate training–testing discrepancies. Their validation MSE steadily declines and then levels off, with no significant fluctuations, suggesting stable learning and reasonable generalization. However, their ultimate error rates remain elevated compared to those of more sophisticated ensemble and kernel-driven models, indicating a restricted ability to fully model the intricate nonlinear interactions present in RABCC-modified concrete mixtures.

The ANN model shows a slight yet steady decrease in both training and validation MSE throughout epochs. Although its convergence lags behind that of tree-based ensembles and GPR, the ultimately attained validation error is competitive. The small and stable gap between training and testing curves suggests that the ANN benefits from appropriate regularization and network architecture, enabling it to learn nonlinear relationships without severe overfitting.

Among all the models, XGBoost showcases one of the most favorable learning behaviors. Following an initial brief transitional period marked by minor variations, both training and validation MSE plummet swiftly and settle at low levels with a comparatively narrow generalization gap. This suggests that XGBoost skillfully manages model complexity and regularization through boosting, shrinkage, and tree pruning, making it well-suited for predictive modeling of concrete CS.

In a similar vein, the ETR model displays robust convergence and minimal validation error, with enhanced generalization compared to RFR. The heightened randomness in feature selection and split thresholds helps mitigate overfitting, yielding smoother learning trajectories and consistent forecasting accuracy.

Fig. 8 presents a comprehensive comparison between measured and predicted 28-day CS values for concrete incorporating RABCC, as obtained from nine machine-learning algorithms. Each subplot illustrates the dispersion of test data around the ideal 1:1 line, together with tolerance bounds corresponding to ±20% (dashed lines) and ±10% (implicitly reflected through the a_{10} metric). The predictive reliability of each model is quantified using the a_{10} and a_{20} accuracy indices, which represent the percentage of predictions that fall within ±10% and ±20% of the measured values, respectively. Collectively, these plots provide an intuitive and quantitative assessment of both accuracy and robustness across the entire strength range.

DTR exhibits the weakest predictive performance among the investigated models. The wide scatter of points around the 1:1 line and the pronounced deviations at both low and high strength levels indicate limited generalization capability. This observation is corroborated by the low a_{10} (40.6%) and a_{20} (74.1%) values, reflecting the inherent tendency of single-tree models to overfit training data while failing to capture smooth nonlinear trends in unseen samples. The noticeable bias at higher CS suggests that DTR struggles to extrapolate beyond densely populated regions of the dataset.

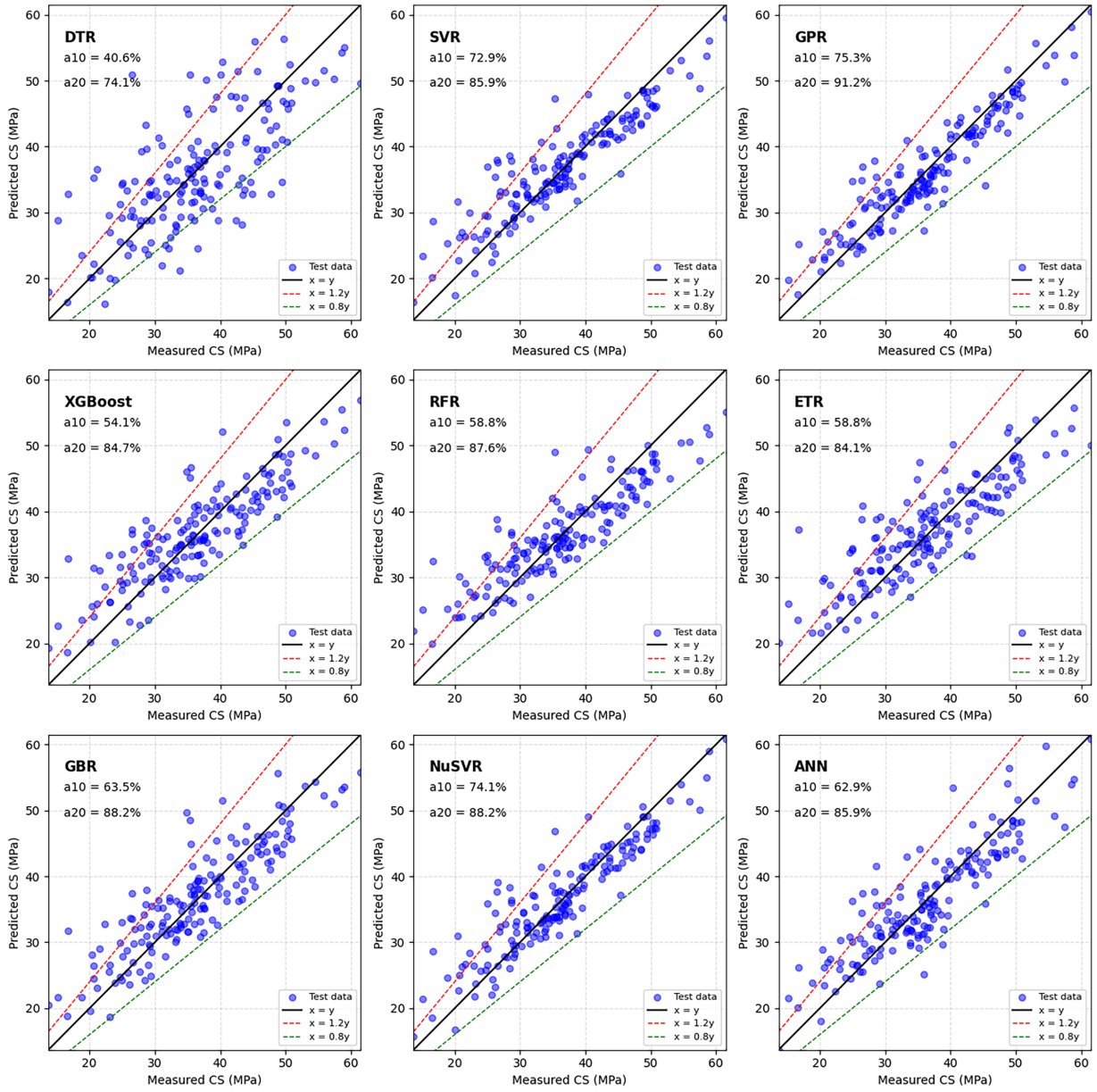

Figure 8: Comparison of machine learning algorithms' performance in predicting the CS of concrete containing RABCC.

SVR significantly improves prediction quality, with data points more tightly clustered around the ideal line. The increased a_{10} (72.9%) and a_{20} (85.9%) values confirm enhanced accuracy and consistency across the dataset. The SVR model effectively captures nonlinear relationships between mix parameters and CS. However, some dispersion remains at higher strength levels, likely due to sensitivity to kernel parameters and limited flexibility in handling highly heterogeneous inputs.

GPR demonstrates the most accurate and stable performance among all models. Predictions are densely concentrated along the 1:1 line over the entire CS range, with minimal bias and reduced variance. This superior behavior is reflected in the highest a_{10} (75.3%) and a_{20} (91.2%) values, indicating excellent predictive reliability. The probabilistic nature of GPR enables it to model complex nonlinear dependencies while

maintaining smoothness and strong generalization, making it particularly suitable for experimental concrete datasets with limited noise.

Ensemble tree-based models show consistently strong performance. XGBoost provides a compact scatter distribution with relatively few outliers, achieving a_{10} and a_{20} values of 54.1% and 84.7%, respectively. Although its a_{10} accuracy is lower than that of kernel-based models, its high a_{20} value demonstrates robust performance within practical engineering tolerance limits. RFR and ETR further improve stability, as evidenced by their balanced point distributions and comparable a_{20} values (87.6% and 84.1%, respectively). These models benefit from ensemble averaging and randomized feature selection, which effectively reduce variance and enhance generalization.

GBR exhibits a notably strong alignment with the 1:1 line, particularly in the mid-strength range. Its relatively high a_{10} (63.5%) and a_{20} (88.2%) values indicate reliable performance with reduced systematic bias. The sequential error-correction mechanism inherent to boosting allows GBR to progressively refine predictions, resulting in a well-balanced trade-off between accuracy and robustness.

The NuSVR model achieves one of the most competitive performances among non-probabilistic approaches, with a_{10} and a_{20} values of 74.1% and 88.2%, respectively. The tight clustering of data points around the ideal line demonstrates its effectiveness in capturing nonlinear relationships while maintaining stability across the dataset. Similarly, ANN yields reasonable predictive accuracy, with a_{10} = 62.9% and a_{20} = 85.9%. While ANN predictions show slightly higher dispersion, especially at extreme strength values, the overall trend remains consistent, confirming the model's capacity to learn complex interactions between input variables.

Table 7 summarizes model performance using multiple complementary statistical indicators, including the coefficient of determination (R^2), root mean square error (RMSE), variance accounted for (VAF), and the a_{20} index, followed by an aggregated scoring and ranking scheme. Among all models, GPR clearly outperforms the others, achieving the highest R^2 (0.88), the lowest RMSE (3.33 MPa), and the highest VAF (0.94). Its a_{20} value of 91.2% further indicates that more than nine out of ten predictions fall within ±20% of the experimental values, which is a strong indicator of engineering reliability. Consequently, GPR attains the maximum total score, confirming its superior generalization capability and robustness.

Table 7: Evaluation and ranking of the machine learning models using statistical criteria under hold-out cross-validation.

	R^2	Score	RMSE (MPa)	Score	VAF	Score	a_{20} (%)	Score	Sum of Scores
GPR	0.88	9	3.33	9	0.94	8	91.2	8	34
NuSVR	0.84	8	3.78	8	0.92	7	88.2	7	30
SVR	0.82	7	4.02	7	0.91	6	85.9	5	25
ANN	0.79	6	4.36	6	0.89	5	85.9	5	22
GBR	0.78	5	4.42	5	0.89	5	88.2	6	21
RFR	0.77	4	4.51	4	0.88	4	87.6	4	16
XGBoost	0.74	3	4.80	3	0.86	3	84.7	3	12
ETR	0.72	2	5.02	2	0.85	2	84.1	2	8
DTR	0.48	1	6.85	1	0.69	1	74.1	1	4

The NuSVR and SVR models rank second and third, respectively. NuSVR demonstrates strong predictive power with R^2 = 0.84 and RMSE = 3.78 MPa, closely followed by SVR (R^2 = 0.82, RMSE = 4.02 MPa). Both models show high VAF values (>0.91) and a_{20} accuracies exceeding 85%, highlighting the effectiveness

of kernel-based approaches in capturing nonlinear relationships between mix design parameters and CS. These results indicate that support vector–based methods provide a favorable balance between accuracy and stability, although they remain slightly inferior to GPR in overall performance.

Ensemble and boosting models exhibit intermediate performance. ANN and GBR achieve comparable results, with R^2 values of 0.79 and 0.78, respectively. While their RMSE values are higher than those of kernel-based models, their VAF and a_{20} metrics remain satisfactory, indicating acceptable predictive capability. RFR and XGBoost further demonstrate moderate performance, benefiting from ensemble learning but with lower accuracy than GBR- and SVR-based approaches. ETR ranks lower, suggesting that excessive randomization may reduce predictive precision for this dataset. DTR performs the poorest, with a substantially lower R^2 (0.48) and the highest RMSE (6.85 MPa), confirming its limited generalization ability when used as a standalone learner.

Fig. 9 complements the numerical rankings by providing residual plots for all models, offering insight into error distribution, bias, and heteroscedasticity. The residuals of the GPR model are tightly clustered around zero across the full range of measured CS values, with no evident systematic trend, indicating unbiased predictions and homoscedastic behavior. This visual evidence strongly supports the statistical dominance of GPR observed in Table 7. Similarly, NuSVR and SVR show relatively narrow residual bands with mild dispersion at higher strength levels, suggesting good generalization with limited bias.

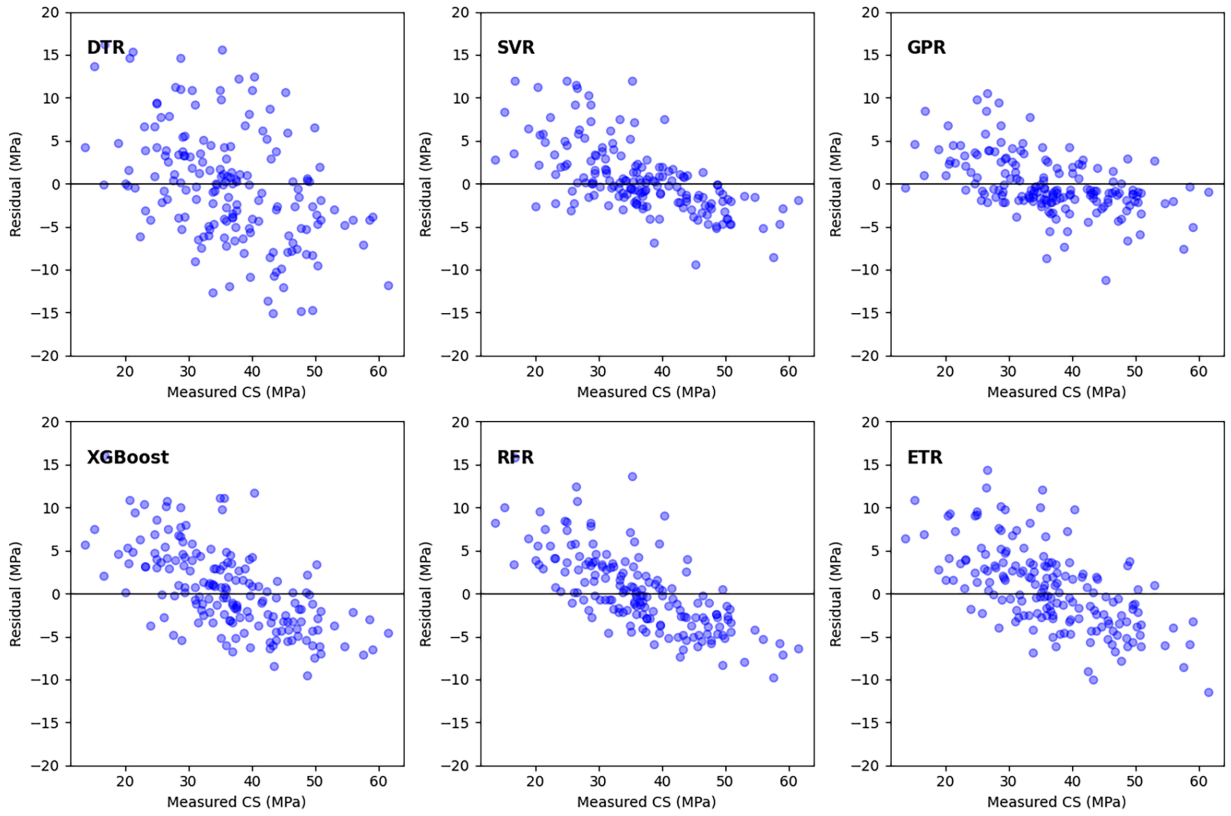

Figure 9: (Continued)

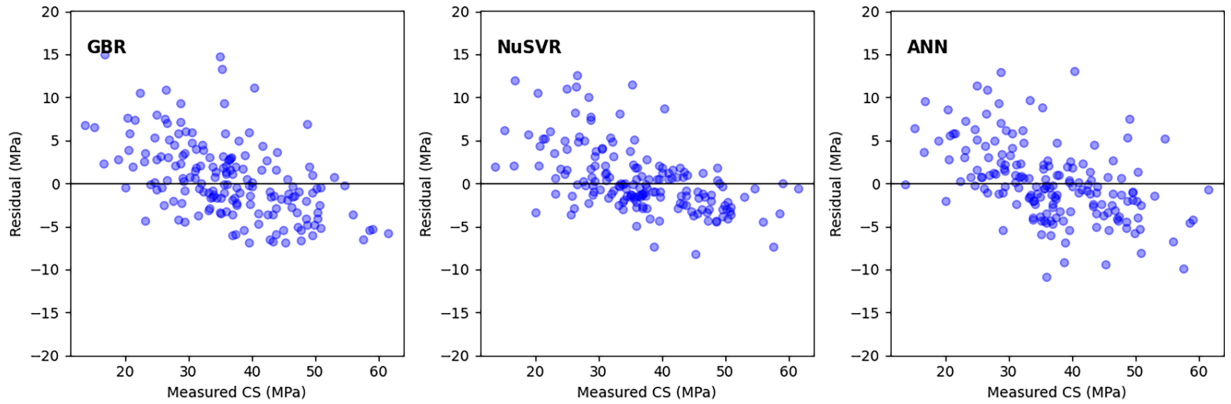

Figure 9: Residual plots of the machine learning models during the hold-out cross-validation.

In contrast, ensemble models such as RFR, ETR, GBR, and XGBoost exhibit wider residual scatter and a noticeable tendency toward negative residuals at higher CS values, indicating slight underestimation of strength in the upper range. While their residuals remain centered around zero overall, the increased spread reflects higher uncertainty and reduced robustness compared to kernel-based models. The ANN residual plot shows moderate dispersion with some clustering, suggesting sensitivity to data distribution and potential overfitting or underfitting depending on the strength range.

DTR residuals display the widest scatter and a clear pattern rather than random dispersion, revealing strong model bias and limited predictive consistency. This behavior corroborates its poor statistical ranking and confirms that simple tree-based models are inadequate for capturing the complex interactions governing CS in RABCC-modified concrete.

5.3 K-Fold Cross-Validation

To further evaluate the robustness and generalization capability of the developed machine learning models, a 5-fold cross-validation strategy was employed. Unlike the hold-out approach, k-fold cross-validation ensures that each data point is used for both training and validation, thereby reducing sampling bias and providing a more reliable assessment of model performance across the entire dataset. Table 8 summarizes the fold-wise results for nine machine learning models in terms of R^2, RMSE, and VAF, along with an aggregated scoring system that enables objective ranking.

Table 8: Evaluation of the machine learning models through several statistical criteria under 5-fold cross-validation.

Model	Fold	R^2	Score	RMSE (MPa)	Score	VAF (%)	Score	Sum of Scores
GPR	1	0.89	7	3.10	9	89.3	9	130
	2	0.94	9	2.37	9	93.8	8	
	3	0.94	8	2.46	9	93.7	9	
	4	0.93	9	2.62	9	92.8	9	
	5	0.92	8	2.75	9	92.4	9	
NuSVR	1	0.84	6	3.77	8	84.3	8	115
	2	0.90	8	3.07	8	89.6	7	
	3	0.89	7	3.19	8	89.3	8	

(Continued)

Table 8 (continued)

Model	Fold	R^2	Score	RMSE (MPa)	Score	VAF (%)	Score	Sum of Scores
	4	0.88	8	3.41	8	87.8	8	
	5	0.88	7	3.43	8	88.2	8	
SVR	1	0.83	5	3.96	7	82.8	7	100
	2	0.87	7	3.44	7	87.1	6	
	3	0.88	6	3.41	7	88.0	7	
	4	0.87	7	3.57	7	86.9	7	
	5	0.87	6	3.65	7	87.0	7	
ANN	1	0.81	4	4.17	6	80.8	6	82
	2	0.86	6	3.55	6	87.1	6	
	3	0.76	4	4.73	4	79.8	5	
	4	0.80	6	4.32	6	81.4	6	
	5	0.81	5	4.41	6	82.9	6	
GBR	1	0.78	3	4.43	5	78.3	5	68
	2	0.77	3	4.57	3	76.9	3	
	3	0.80	5	4.34	6	80.4	6	
	4	0.79	5	4.46	5	79.1	5	
	5	0.80	4	4.51	5	79.7	5	
ETR	1	0.78	3	4.46	3	77.9	3	59
	2	0.81	5	4.13	5	81.1	5	
	3	0.78	3	4.53	5	79.4	4	
	4	0.76	4	4.76	4	76.2	4	
	5	0.77	3	4.77	4	77.2	4	
RFR	1	0.78	3	4.45	4	78.0	4	50
	2	0.78	4	4.41	4	78.5	4	
	3	0.78	3	4.52	3	78.9	3	
	4	0.74	3	4.93	3	74.5	3	
	5	0.77	3	4.79	3	77.0	3	
XGBoost	1	0.68	2	5.42	2	68.6	2	30
	2	0.70	2	5.16	2	70.7	2	
	3	0.66	2	5.69	2	66.1	2	
	4	0.59	2	6.28	2	58.6	2	
	5	0.73	2	5.23	2	72.5	2	
DTR	1	0.47	1	6.89	1	48.1	1	15
	2	0.36	1	7.60	1	36.0	1	
	3	0.56	1	6.48	1	57.7	1	
	4	0.47	1	7.08	1	48.2	1	
	5	0.46	1	7.36	1	45.8	1	

Among all models, GPR consistently performs best across all five folds. Its R^2 values range from 0.89 to 0.94, while RMSE remains remarkably low (2.37–3.10 MPa), indicating excellent predictive accuracy and minimal dispersion across different training–testing splits. The VAF values exceeding 92% in all folds further confirm that GPR effectively captures the underlying nonlinear relationships governing the CS of RABCC-modified concrete. The highest cumulative score (130) reinforces GPR's stability, robustness, and strong generalization capability.

The NuSVR model ranks second, demonstrating consistently high predictive performance, with R^2 values between 0.84 and 0.90 and RMSE values ranging from 3.07 to 3.77 MPa. Its VAF values (84.3%–89.6%) indicate reliable variance explanation across folds. The relatively minor fluctuations in performance metrics suggest that NuSVR maintains good stability across different data partitions, making it a competitive alternative to GPR, albeit with slightly lower accuracy.

The standard SVR model also performs well, achieving R^2 values of around 0.88 in its best folds and RMSE values of 3.41–3.96 MPa. However, compared to NuSVR, SVR exhibits marginally higher prediction errors and lower cumulative scores (100), suggesting reduced flexibility in capturing the complex interactions between RABCC–C, mixture proportions, and curing parameters.

ANN demonstrates moderate predictive capability, with R^2 values ranging from 0.76 to 0.86. While ANN models can learn nonlinear trends, their performance is less consistent across folds, as evidenced by fluctuating RMSE and VAF values. This variability indicates sensitivity to data partitioning and network initialization, which may limit their robustness on this dataset.

Ensemble tree-based models show mixed performance. GBR achieves stable but moderate accuracy (R^2 = 0.77–0.80), benefiting from its sequential learning strategy. ETR and RFR exhibit similar behavior, with R^2 values generally below 0.81 and higher RMSEs than kernel-based models. Although ensemble averaging reduces variance, excessive randomization (particularly in ETR) appears to limit predictive precision for concrete containing RABCC.

XGBoost, despite its reputation for high predictive power, exhibits comparatively lower performance in this study. Its R^2 values range from 0.59 to 0.73, and RMSE values exceed 5 MPa in most folds, indicating difficulty in capturing the experimental response surface. This suggests that the dataset structure and feature interactions favor probabilistic and kernel-based approaches over highly aggressive boosting strategies.

As expected, DTR performs the weakest, with low R^2 values (0.36–0.56), high RMSE values (>6.48 MPa), and the lowest cumulative score (15). These results confirm the limited generalizability of single-tree models and their susceptibility to overfitting in modeling complex, nonlinear material behavior.

5.4 Statistical Significance Testing

To statistically verify whether the observed performance differences among the machine learning models are meaningful, a non-parametric Friedman test followed by a critical difference (CD) analysis was conducted. Fig. 10 presents the CD diagram, which ranks the models based on their average performance across the validation folds, with lower ranks indicating superior predictive accuracy.

The Friedman analysis reveals a clear separation between high-performing and low-performing models. GPR achieves the best average rank, confirming its dominant predictive capability. NuSVR and SVR follow closely, forming a statistically competitive group with GPR. The proximity of these models within the CD threshold (CD = 5.37) indicates that their performance differences are not statistically significant, suggesting that all three kernel-based methods offer comparable reliability for CS prediction. ANN and GBR occupy intermediate ranks, reflecting moderate predictive performance. While kernel-based approaches outperform these models, their ranking suggests acceptable accuracy for applications where computational simplicity

or interpretability is prioritized. ETR and RFR rank lower, indicating reduced effectiveness relative to the leading models, although they remain superior to simpler learners. XGBoost and DTR appear at the worst end of the ranking spectrum. Their average ranks fall well outside the CD threshold when compared to GPR and NuSVR, confirming that their inferior performance is statistically significant rather than incidental. This outcome reinforces the conclusion that aggressive boosting and single-tree approaches are less suitable for modeling the nonlinear, material-dependent behavior of RABCC-modified concrete.

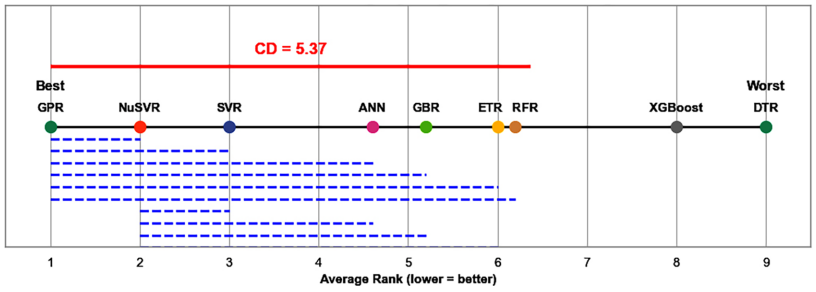

Figure 10: CD diagram of the machine learning models based on Friedman–Nemenyi analysis.

The horizontal blue dashed lines represent clusters of machine learning models whose mean ranks reside within CD = 5.37. Models linked by the identical dashed segment cannot be regarded as statistically distinct in their performance at the selected significance threshold (commonly $\alpha = 0.05$), even when their average ranks differ numerically. In other words, although one model may appear slightly better or worse in ranking, the observed difference may be due to random variation rather than a true performance gap. The dashed lines indicate that GPR, NuSVR, SVR, ANN, and GBR fall within intersecting CD ranges, suggesting statistically similar predictive capabilities across these algorithms. This clarifies why, despite GPR achieving the top average rank, its dominance over NuSVR and SVR is not statistically significant under the Friedman–Nemenyi test. On the other hand, models like XGBoost and DTR, which are not linked to the foremost group by dashed lines, show statistically poorer performance, confirming that their lower rankings are meaningful rather than due to chance.

6 SHAP Analysis

SHAP analysis is a key step in bridging the gap between the high performance of machine learning models and engineering interpretability. Complex models like GPR can capture the nonlinear relationship between the mix design parameter and CS. Still, their inner workings remain unknown. SHAP analysis is based on game theory and provides a valuable way to decompose the model's prediction, adding each user's input as additive features for local and global interpretability. In civil and materials engineering, this is a highly desirable feature but a clear drawback in practice. Trust in the model's operations is kept under check, and transparency, care in understanding from a physical point of view, and interpretability were considered critically important. SHAP allows engineers to evaluate model outputs against established principles of concrete technology by quantifying the direction and magnitude of feature impacts. This quantification empowers engineers to develop, among other advantages, the significant driving parameters, the nonlinear interactions among these parameters, and actionable interpretations of the mix design. Therefore, SHAP analysis facilitates the transformation from purely predictive models to decision-support systems by using machine learning models suitable for performance-based concrete design.

Residual distribution of the GPR model, as the deviation between experimental and the respective model-predicted CS values, appears in Fig. 11. The histogram accompanied by a superimposed kernel density

curve presents an approximately symmetrical and bell-shaped distribution, centered close to zero in residual. This indicates that the GPR model is essentially unbiased, showing no substantial systematic tendency toward over- or underprediction across the sample. The greatest number of residuals fall within a small range of about ±5 MPa, thereby confirming the model's high precision and strong generalization. The residual tails taper away gradually, indicating that the frequency of prediction errors is on the rare side, further confirming the robust interaction of the GPR in modeling CSs of concrete mixtures with RABCC. With this statistical standpoint, the normality of residuals further guarantees that the assumptions are being met correctly and that the nonlinearity in predominant input variables associated with CS has been significantly captured.

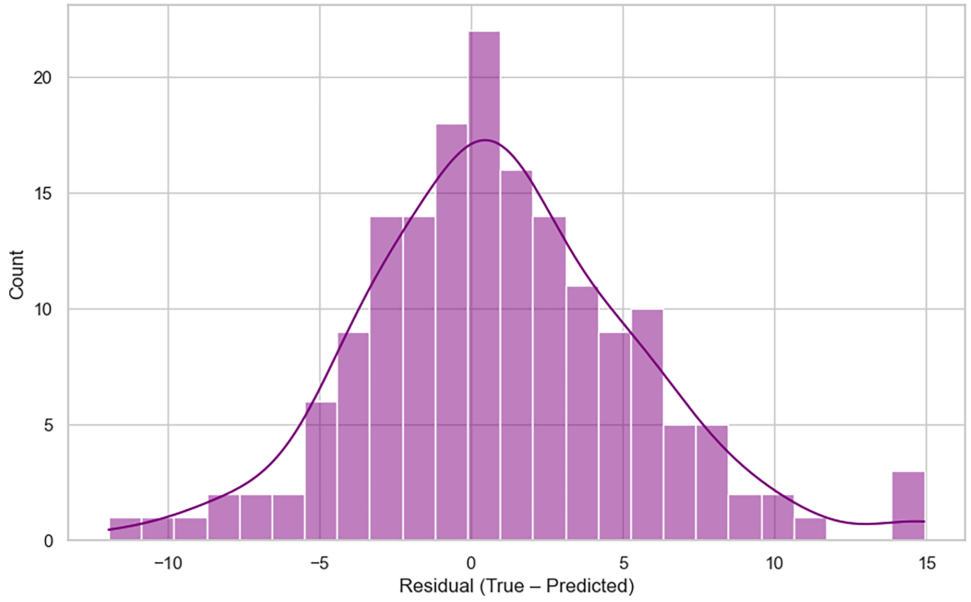

Figure 11: Residual distribution diagram for the GPR model.

The local force plot (Fig. 12) for Sample A provides an intricate set of explanations to examine the effects of individual parameters on the predicted CS value relative to the model's base value. In this case, negative influences, which also appear in blue, dominate the output, pulling it downward relative to the baseline. Noteworthy is that an extremely high w/c ratio (0.554) plays a powerful negative role in the output, which is not unexpected given that its negative value is well established. Also, higher FAC and CAC contribute to strength reduction; probably, the effect combines the amount with the availability of paste at the time of curing and packing of the aggregate. The lower silica fume content (SFC = 0.25%) has a somewhat smaller impact on strength reduction, indicating that its dosage here is insufficient to offset the adverse effects of the other factors considered. Just the desired CT (28 days) and the SPC make a minor contribution to the enhancement of strength, but the countervailing effect of other negative influences negates these. Overall, Sample A represents a mixture configuration in which low water content and aggregate proportions attenuate the beneficial effects of the admixtures, and curing is insufficient to predict a relatively lower CS.

Sample B (Fig. 12) shows a completely opposite trait, with a positive contribution from the red-colored feature, resulting in a good force plot that pushes its way above the baseline. Here, with a moderate w/c ratio (0.519) the harmful effect is not that much. Concomitant values of RABCC–C with an R-factor of 2.0% and SPC (that is 0.833%) contribute rather positively to enhanced workability and better particle dispersion. Terrain is thereby balanced in authority, thereby providing the dualistic view of better interaction between the components supported by the concrete matrix. Also, SFC of 3.61% follows in the enhancing gear,

imparting higher strength gain to CS due to internal pore-structure modification and increased ITZ. The combined positive contributions result in a high predicted CS, illustrating that carefully controlled RABCC incorporation, when synergistically combined with supplementary cementitious materials and adequate chemical admixtures, can yield concrete mixtures that are both mechanically efficient and sustainable.

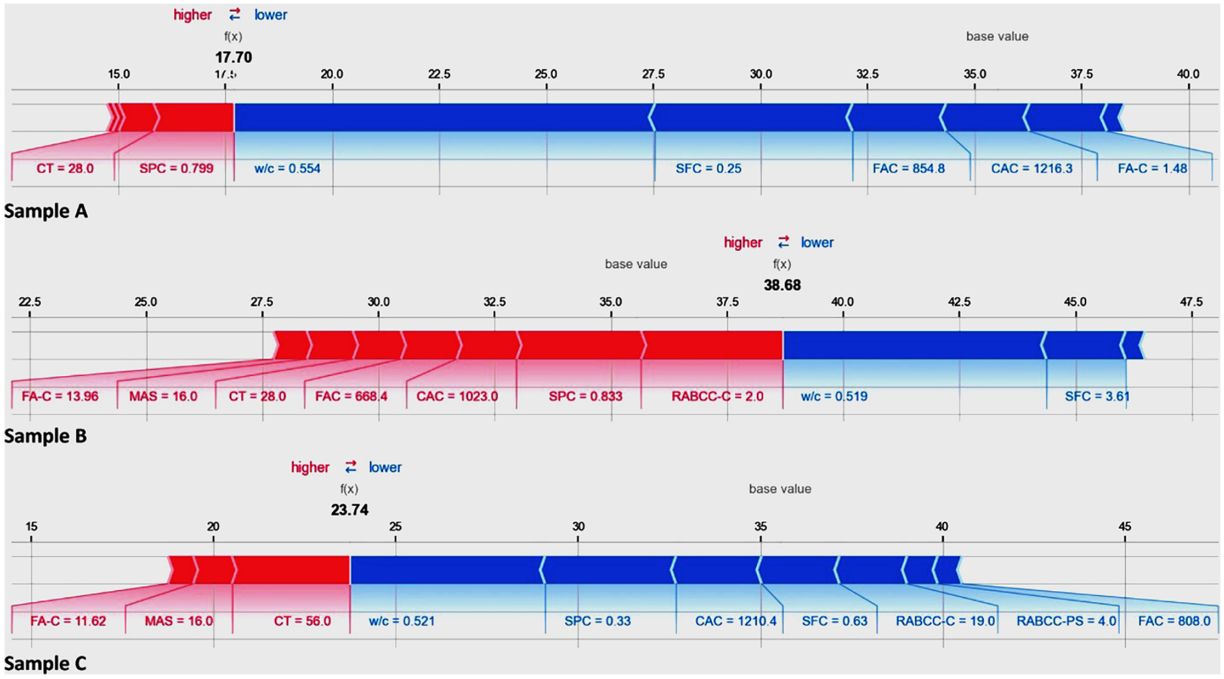

Figure 12: Force plot for a local interpretation of three sample points (A, B, and C) using the GPR model.

The test data from Sample C (Fig. 12) emphasize the undesirable effects of incorporating higher RABCC into concrete. While the use of the extended CT (56 days) fosters appreciable strength generation, this increase is offset by the high RABCC-C content (19.0%) and the presence of giant-sized RABCC particles (RABCC–PS = 4.0 mm). These factors substantially reduce the predicted CS in a manner that provides a weaker interfacial transition zone, fosters increased porosity, and raises additional stress-concentration sites, possibly associated with metal inclusions, contributing to these harmful effects by picking up on FAC. While moderate w/c ratio and SPC provide limited positive effects, they are overwhelmed by the adverse influence of excessive aluminum crumb content. This sample clearly illustrates the nonlinear threshold behavior of RABCC, confirming that beyond an optimal range, its inclusion leads to pronounced mechanical degradation.

The plot shown in Fig. 13 is the comprehensive global SHAP summary visualization for the GPR model, providing a concise yet insightful depiction of both feature significance and the directional impact each variable has on CS. The features are ordered from top to bottom by their mean absolute SHAP values, thereby illustrating their overall relative contribution to the model's predictions. In line with traditional concrete mechanics and previous correlation findings, the w/c ratio stands out as the most pivotal factor. Elevated w/c ratios (highlighted in red) predominantly correspond to negative SHAP scores, signifying a marked decrease in CS, whereas reduced w/c ratios (blue) provide a beneficial effect. This consistent, distinctly segregated pattern underscores the leading, physically meaningful role of w/c ratio in controlling strength development and confirms that the GPR model accurately encapsulates this essential relationship.

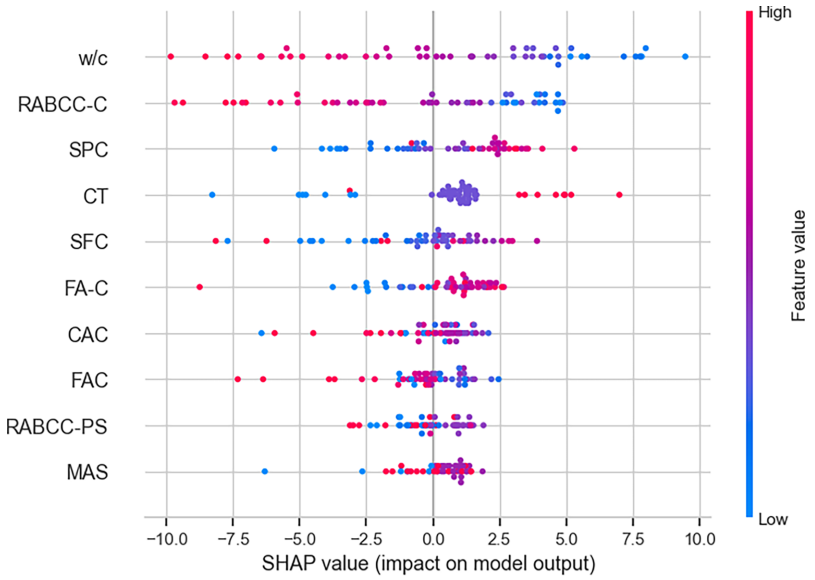

Figure 13: Global SHAP values based on the GPR model.

RABCC–C claims the second spot in feature influence, highlighting its crucial role in CS. The chart demonstrates a distinct trend where elevated RABCC–C amounts (red markers) tend to have adverse effects, while smaller quantities (blue markers) correlate with positive or nearly neutral SHAP values. This pattern illustrates the complex nature of RABCC inclusion: at minimal levels, its impact on strength is marginal, but surpassing a certain point, detrimental effects linked to increased porosity, diminished stiffness, and fragile interfacial transition zones become prevalent. The comparatively broad horizontal dispersion of SHAP values for RABCC–C signifies a significant nonlinear interplay with other mixture variables, including the w/c ratio and SPC.

SPC ranks third in importance and primarily exerts a favorable influence at higher concentrations. Points colored red for SPC generally fall on the positive SHAP side, validating that boosting SPC improves workability, compaction efficiency, and ultimately CS. This tendency is especially notable in RABCC-modified mixtures, where increased admixture is often necessary to counterbalance the adverse rheological effects introduced by metallic crumbs. CT also exhibits a positive influence over extended durations, as prolonged curing consistently shifts SHAP values upward, reflecting ongoing hydration and microstructural enhancement.

SFC exerts a moderate yet significant effect, where greater quantities typically enhance CS. The variability observed reflects interplay-driven fluctuations, which is expected given how sensitive silica fume's effectiveness is to dosage, curing duration, and water content. Features of FA–C, CAC, and FAC fall within a moderate to low significance range. Their SHAP value distributions are fairly tight and hover around zero, implying that although they affect CS, their impact is secondary and often contingent on specific conditions rather than universally dominant. Lastly, RABCC–PS and MAS show the least influence, signifying that within the studied ranges, their roles in CS prediction are relatively minor compared to mixture ratios and binder-related factors.

Fig. 14 presents a SHAP heatmap that complements the overall summary plot by showing how each feature's contribution varies across individual samples. Each column represents a concrete blend, while each row corresponds to a specific feature, with color intensity indicating the strength and direction of the SHAP

value. Above, the line plot displays the model's output. $f(x)$ shows the predicted CS trend across instances, enabling a direct visual linkage between prediction magnitude and feature-level contributions.

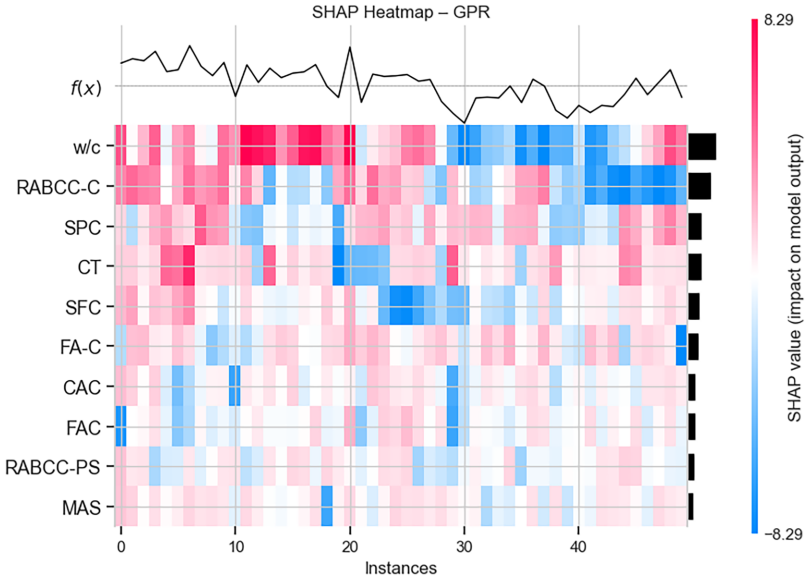

Figure 14: SHAP heatmap based on the GPR model.

The heatmap displays organized patterns rather than random noise, validating that the GPR model has captured stable, physically significant connections. In the top rows, w/c and RABCC–C demonstrate pronounced and coherent color shifts. Instances linked with lower predicted CS feature vivid blue zones for w/c and RABCC–C, signaling adverse effects stemming from elevated water content or excessive aluminum crumb inclusion. In contrast, strength predictions align with red or pink hues, indicating low w/c ratios and moderated RABCC levels. These trends support the inference that these two factors function as the key controlling variables for CS within the dataset.

SPC and CT exhibit alternating yet predominantly favorable influences across high-strength instances, as evidenced by recurrent red bands aligned with elevated model outputs. This verifies that admixture dosage and CT serve as balancing factors, partially offsetting the adverse impacts of other variables. SFC also reveals concentrated red areas, especially in cases with higher predicted CS, underscoring its significance in enhancing microstructural compactness and progression of strength when administered correctly.

Features of lower rank, such as FA–C, CAC, FAC, RABCC–PS, and MAS, exhibit more scattered and subdued color manifestations, suggesting weaker, more interaction-based effects. Their contributions hover around zero, indicating that they adjust rather than overwhelm the CS response. Crucially, the lack of sudden or irregular color shifts reinforces the numerical robustness of the GPR model and demonstrates that no individual feature exerts an exaggerated or undue effect on isolated predictions.

Fig. 15 depicts the SHAP dependency and interaction plots generated by the GPR model, providing an in-depth, mechanistic explanation of how the w/c ratio interacts with other input variables to affect the predicted CS. In all subplots, the horizontal axis represents the w/c ratio, while the vertical axis denotes the corresponding SHAP value of w/c, i.e., its marginal contribution to the model output. The color scale in each panel represents the interacting feature, allowing a simultaneous evaluation of both the primary impact of w/c and its interaction with additional mix-design parameters. Across all interaction plots, a remarkably consistent and strongly monotonic trend is observed. As the w/c ratio rises, the SHAP value of w/c declines

sharply from positive to negative. This pattern validates that w/c is the key controlling factor in the GPR model, imposing a systematic and physically significant influence on CS. At low w/c values (roughly 0.30–0.40), SHAP values are primarily positive, signifying a notable improvement in CS. Beyond a critical point (near w/c ≈ 0.48–0.50), SHAP values turn increasingly hostile, indicating swift strength degradation. The smooth, continuous decline underscores the GPR model's ability to capture nonlinear yet stable relationships without introducing artificial breaks.

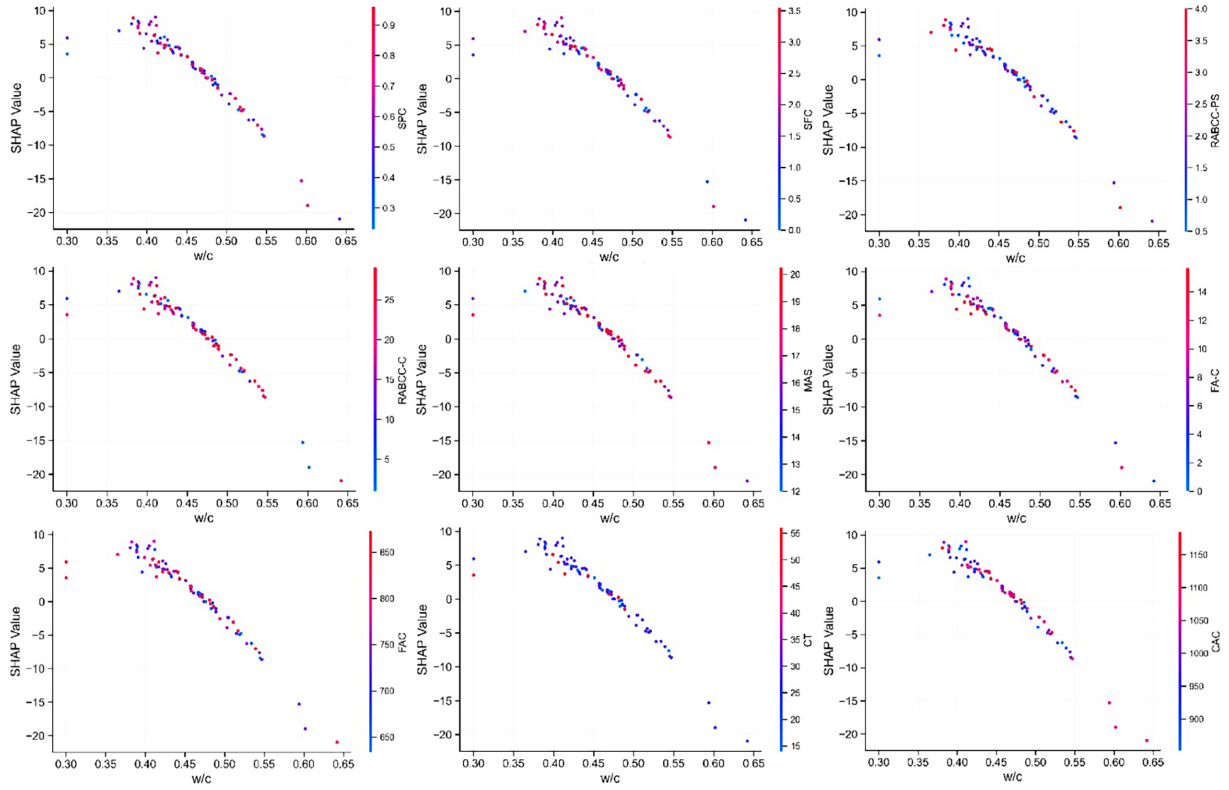

Figure 15: SHAP dependency and interaction plots based on the GPR model.

The interaction between w/c and SPC, SFC, and RABCC–PS illustrates how admixture- and microstructure-related factors moderate the negative effects of increasing w/c ratio. For SPC and SFC, higher values (shown by warmer colors) tend to correspond with less negative SHAP values at similar w/c levels. This implies that sufficient amounts of chemical and mineral admixtures can partly offset the strength reduction caused by higher water content, likely through enhanced particle packing, improved workability, and a refined pore structure. In contrast, changes in RABCC–PS have a comparatively minor moderating effect, as indicated by the narrow color range along the main SHAP trend, suggesting that particle size plays a lesser role than mixture proportions.

The interaction diagrams featuring RABCC–C, MAS, and FA–C highlight the interconnected essence of strength evolution. Elevated RABCC–C amounts correspond with more negative SHAP values at increased w/c ratios, signifying a combined declining impact when surplus water content and greater RABCC–C occur simultaneously. This interaction is consistent with increased porosity and weaker interfacial transition zones under such conditions. Equally, changes in MAS reveal that bigger aggregate sizes generally intensify the negative influence of high w/c slightly, though the magnitude remains modest. FA–C shows a varied trend, where increased FA–C values tend to mitigate strength reduction at moderate w/c levels but become less

effective at significantly elevated w/c ratios, highlighting that fly ash pozzolanic activity depends on sufficient curing and water regulation.

The interaction plots in the bottom row concerning FAC and CAC reveal relatively subtle color gradients, indicating weak secondary interactions with w/c. While aggregate proportions affect packing density and load transmission, their influence is vastly surpassed by the predominant role of w/c. The clustering of data points along a single downward curve indicates that aggregate content primarily serves as a fine-tuning parameter rather than a primary driver of CS variability in the studied domain.

7 Uncertainty Quantification

Quantifying uncertainty is crucial in contemporary data-centric modeling, especially in civil and materials engineering, where experimental fluctuations, measurement noise, and intrinsic material diversity are inescapable. Beyond simple point estimates, uncertainty quantification offers a probabilistic perspective on model reliability, enabling researchers and professionals to distinguish dependable outputs from areas of increased epistemic or aleatory uncertainty. Regarding concrete strength estimation, uncertainty quantification aids risk-aware decision-making by estimating the probability of underestimation or overestimation, which is vital for structural safety, quality assurance, and resilient mix design optimization. Furthermore, integrating uncertainty data boosts model openness and trustworthiness, enables comparative evaluation among competing models, and harmonizes machine learning results with reliability-oriented design principles commonly embraced in structural engineering.

Fig. 16 presents a detailed comparison between the experimentally measured CS values, the GPR model predictions, and the associated bootstrapped 95% confidence intervals (CIs) across the test dataset. The horizontal axis represents individual test samples, while the vertical axis denotes CS in MPa. The actual values (blue markers) and GPR predictions (red markers) exhibit strong visual agreement throughout the entire sample range, indicating the high predictive fidelity of the GPR model. The close tracking of the red prediction curve to the blue experimental data highlights the model's capability to capture both the central tendency and the rapid local fluctuations in CS arising from variations in mix proportions and curing conditions.

The shaded green bands correspond to the bootstrapped 95% CIs, which provide a quantitative measure of predictive uncertainty around the GPR estimates. For the majority of test samples, the experimental CS values fall well within the predicted confidence bounds, demonstrating that the uncertainty estimates are well calibrated and statistically meaningful. This behavior suggests that the model not only achieves high accuracy but also reliably characterizes the dispersion associated with its predictions, a key requirement for trustworthy deployment in engineering applications.

Looking more closely, it becomes clear that the CI widths vary among samples. Slimmer confidence bands emerge in areas where the model likely encountered plentiful, representative training data, indicating low epistemic uncertainty and firm trust in the forecasts. Conversely, broader CIs encompass specific samples exhibiting sudden strength fluctuations or extreme CS readings, signaling heightened uncertainty. These localized swells in the CI bounds are physically justifiable, since such samples may relate to rare parameter mixes (e.g., elevated RABCC–C or extreme w/c ratios) where data scarcity or greater variability is anticipated.

Importantly, even in cases where prediction errors are relatively larger (such as sharp peaks or troughs in CS), the true values generally remain within or very close to the 95% CI bounds. This indicates that deviations between predicted and observed values are largely attributable to intrinsic material variability rather than systematic model bias. The absence of persistent underestimation or overestimation trends across the test samples further confirms the robustness and unbiased nature of the GPR model.

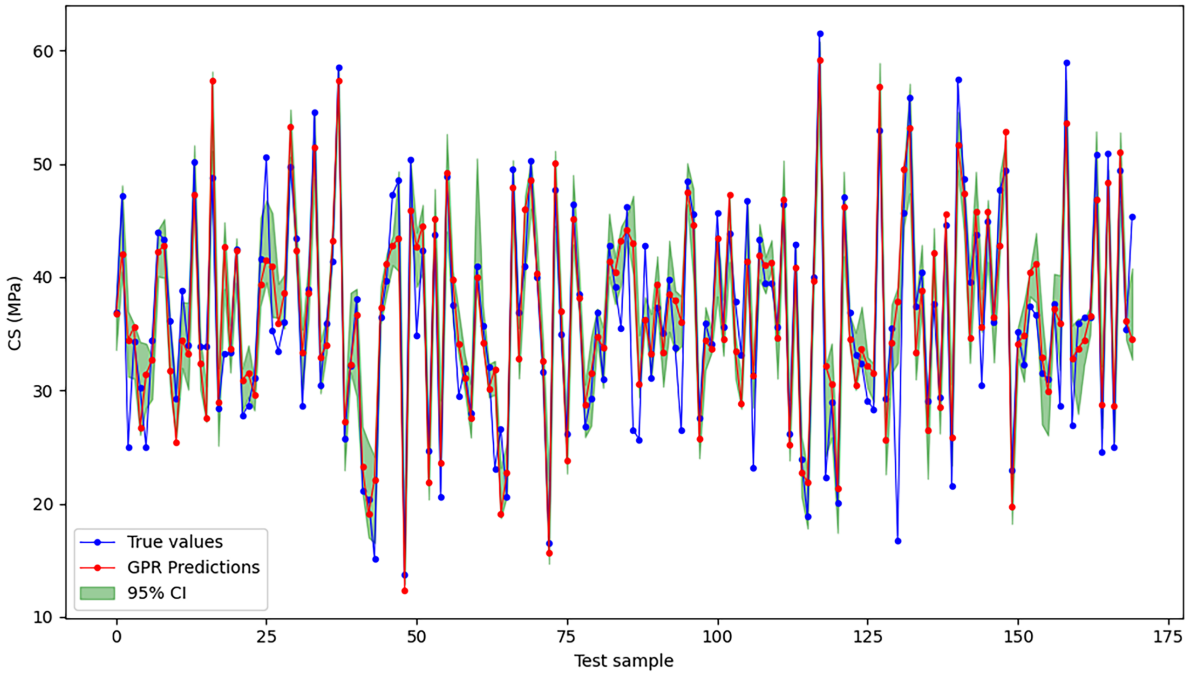

Figure 16: GPR predictions with bootstrapped 95% CIs.

Fig. 17 illustrates the statistical distribution of predictive uncertainty quantified by the standard deviation of the GPR model predictions. The bar chart shows that prediction uncertainty values mostly cluster within a fairly tight range spanning roughly from 4.1 to 4.4 MPa, signifying consistent and reliable predictive confidence across most of the dataset. The distribution skewing rightward illustrates that only a small fraction of samples present heightened uncertainty levels exceeding about 4.6 MPa. These elevated uncertainty instances likely correspond to mixtures with boundary conditions or less densely sampled regions of the feature space, such as elevated RABCC replacement percentages or rare parameter combinations. The lack of overly wide uncertainty spread suggests the GPR model maintained well-regulated epistemic uncertainty throughout its prediction range. Therefore, the illustration confirms that the uncertainty-aware GPR framework delivers not only precise predictions but also statistically sound confidence assessments capable of underpinning reliability-focused engineering decisions.

Fig. 18 illustrates the relationship between predictive uncertainty and the absolute prediction error generated by the GPR model. The scatter plot reveals that samples linked with comparatively larger prediction errors tend to align with elevated uncertainty values, indicating that the uncertainty quantification framework is both physically relevant and accurately calibrated. Most data points are grouped within low to moderate error ranges, generally below around 5 MPa, accompanied by uncertainty levels ranging from approximately 4.1 to 4.4 MPa, which confirms consistent predictive performance across most mixtures. A small set of outlier points show higher absolute errors, especially in areas with increased uncertainty, which is expected for intricate or underrepresented mixture setups. Importantly, the lack of a systematic concentration of high-error samples at low uncertainty values suggests that the GPR model successfully identifies regions where prediction confidence should be lowered. This pattern demonstrates the capability of the uncertainty-aware framework to differentiate between highly dependable predictions and those linked to heightened variability or limited training data coverage. Consequently, the figure emphasizes the practical engineering significance of integrating predictive precision with uncertainty estimation when assessing sustainable concrete materials incorporating RABCC.

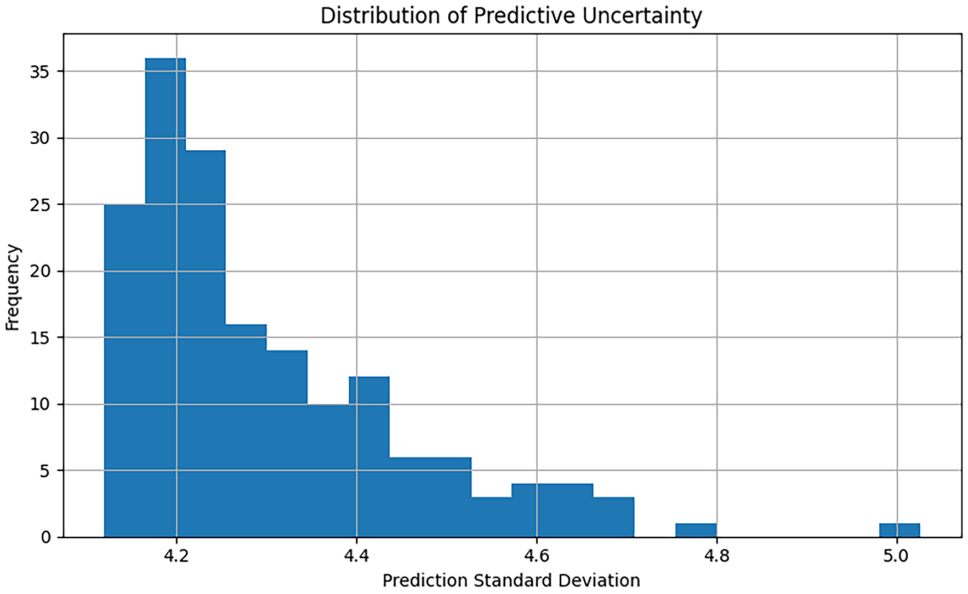

Figure 17: The distribution of prediction standard deviations obtained from the GPR model for CS prediction of RABCC concrete.

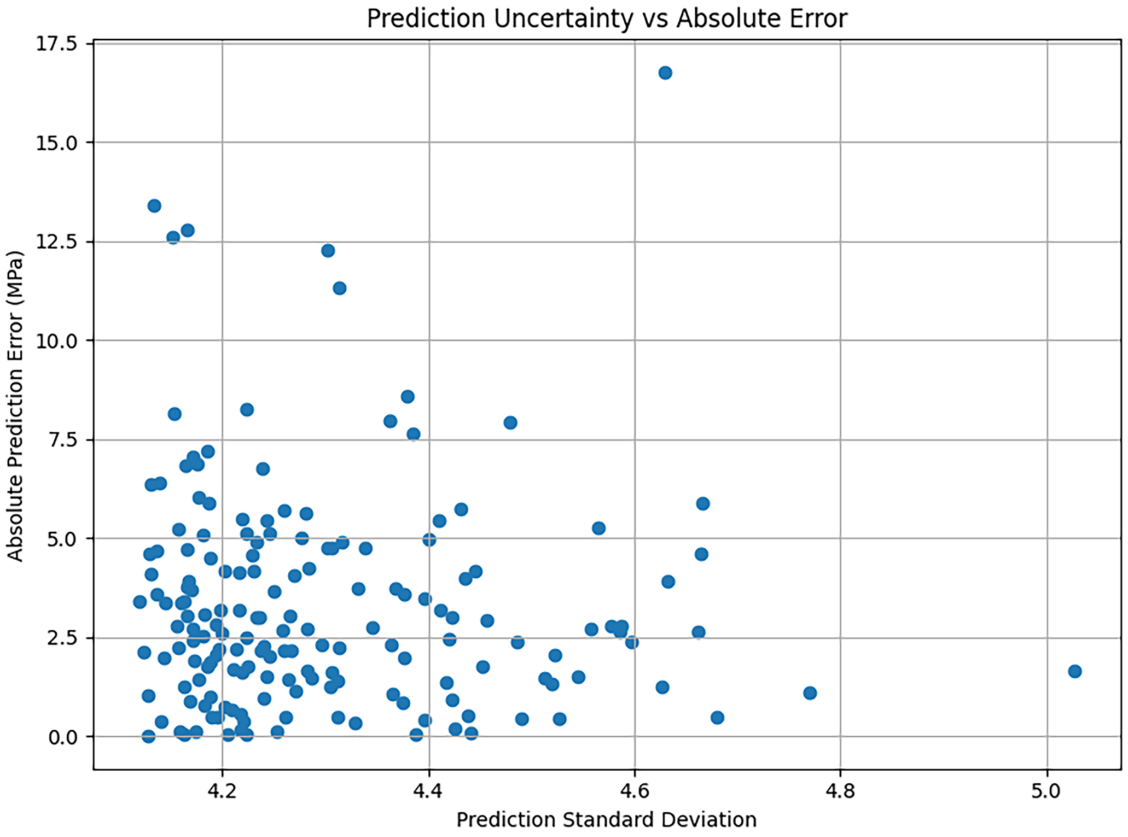

Figure 18: The relationship between absolute prediction error and prediction standard deviation for the GPR model.

8 Key Limitations and Suggestions

The models applied mainly comprised traditional regression and tree-based methods, whereas newer deep-learning and attention-driven designs including transformer networks, graph neural networks, and physics-informed deep learning frameworks were excluded from examination. While the chosen models were deemed suitable for the scale and makeup of the current experimental database, cutting-edge deep-learning techniques could provide enhanced ability to uncover highly intricate nonlinear relationships and multiscale dependencies in larger and more diverse concrete datasets. Hence, upcoming studies should focus on incorporating attention-based and deep-learning methods, especially as expanded multi-source datasets become accessible, to significantly improve predictive precision, feature interplay analysis, uncertainty quantification, and multi-objective optimization of sustainable concrete utilizing recycled aluminum materials.

While the experimental and machine learning findings offer valuable insight into the CS behavior of RABCC concrete, this current study did not employ direct microstructural characterization methods such as SEM, EDS, XRD, or FTIR. As a result, the suggested mechanisms involving interfacial transition zone behavior, porosity evolution, hydration-product interactions, and aluminum-induced microstructural modifications remain speculative. To confirm these relationships, future research should integrate detailed microstructural analyses to directly link RABCC inclusion with the physicochemical processes that dictate concrete performance.

Even though the crafted machine learning algorithms exhibited robust forecasting capabilities within the generated experimental database, the current investigation did not carry out external validation using separately created datasets. Therefore, it is advised to pursue further multi-source experimental confirmation before applying the developed models more broadly to wider practical scenarios or distinct material situations.

The current research mainly examined the CS characteristics and machine learning-driven forecasting of concrete embedded with RABCC. Although CS is a key engineering performance indicator, other durability factors such as water absorption, permeability, chloride penetration resistance, sulfate resistance, shrinkage, freeze–thaw durability, and corrosion behavior were not tested experimentally. Thus, the suggested guidelines for structural use should be deemed tentative and confined to the mechanical properties investigated. Subsequent research must include in-depth durability evaluations, microstructural analysis, and extended environmental exposure studies to robustly confirm the structural feasibility and enduring performance of RABCC concrete.

The experimental database utilized in this research was constructed under fairly controlled laboratory environments employing distinct material sources, curing conditions, and batching methods. As a result, some real-world variability elements such as changes in raw material characteristics, environmental exposure, moisture levels, field compaction techniques, temperature shifts, and inconsistencies in large-scale production were not fully captured in the present dataset. Hence, although the developed machine learning models showed strong predictive accuracy within the studied parameters, prudence is advised when applying these results to significantly different field settings or material origins. Future studies should aim at creating expansive multi-source datasets that embrace wider environmental, geographic, and material diversity to enhance the robustness, adaptability, and practical generalization of the proposed predictive system.

While this research mainly concentrated on the mechanical attributes and machine learning-driven forecasting, the addition of RABCC could also offer significant environmental advantages. Using RABCC to partially substitute natural aggregates can curtail the use of virgin aggregate materials and redirect aluminum waste away from landfills, thus promoting sustainable waste management and circular economy-centric construction methods. Hence, incorporating recycled aluminum waste into concrete might indirectly

help decrease the environmental impact of construction materials. However, the environmental advantages outlined here are mainly qualitative, as a full life-cycle assessment (LCA), embodied carbon evaluation, and economic sustainability analysis were outside the purview of this study. Future investigations should aim to combine comprehensive environmental and techno-economic analyses to rigorously assess the sustainability of RABCC concrete in real-world engineering scenarios.

9 Conclusions

This research comprehensively analyzed the viability and effects of integrating RABCC into concrete blends, with CS as the primary performance metric. The findings revealed that RABCC, when utilized as a partial substitute for NCA, can enhance the sustainability of concrete manufacture without notably diminishing its strength, provided the addition is precisely regulated.

The experimental findings indicated that low levels of RABCC incorporation (up to 5%) had minimal effects on CS, with only a slight reduction. At these lower replacement levels, the CS values were comparable to those of the reference mix, which had a CS of 42.1 MPa. For instance, at 2.5% RABCC replacement, the CS reduced to 41.0 MPa, and at 5% RABCC replacement, the CS reduced to 38.7 MPa. However, at higher replacement levels, such as 10% and beyond, a more significant decline in CS was observed. For example, at 12% RABCC, the CS decreased to 34.5 MPa, and at 20% RABCC, the CS was further reduced to 29.5 MPa. These results highlighted the nonlinear relationship between RABCC–C and CS, where the benefits of recycling are balanced by the negative impact on the structural integrity of concrete at higher inclusion levels.

The machine learning models, including GPR, SVR, NuSVR, DTR, XGBoost, RFR, ETR, ANN, and GBR were employed to predict the CS of concrete based on various mix parameters, including RABCC–C, RABCC–PS, w/c ratio, SPC, SFC, FAC, CAC, FA–C, MAS, and CT. The model's performance was rigorously evaluated using hold-out testing and 5-fold cross-validation. The GPR model demonstrated the most robust results. In the hold-out validation, the GPR model achieved an R^2 of 0.88 and an RMSE of 3.33 MPa, demonstrating good predictive accuracy for CS. The 5-fold cross-validation further validated GPR's robustness relative to other models, with R^2 values of 0.89–0.94, RMSE values of 2.37–3.10 MPa, and VAF values of 89.3%–93.8%. These results confirmed the suitability of machine learning, particularly GPR, for accurately predicting CS in concrete mixes with varying RABCC levels, making it a reliable tool for optimization and decision-making in concrete mix design.

In addition to GPR, a SHAP assessment was conducted to evaluate the influence of each feature on the model's output. The evaluation showed that the w/c ratio was the key feature impacting the CS, followed by RABCC–C. The w/c ratio exerted a notably adverse effect on the CS, whereas RABCC–C demonstrated a moderately negative association, supporting the results observed in the experimental data. SPC and CT were also recognized as key factors affecting strength development, particularly in terms of workability and long-term hydration of the concrete.

The findings of this study provide valuable insights into the potential to integrate recycled materials such as RABCC into concrete for sustainable construction. While the incorporation of RABCC offers significant environmental benefits, especially in terms of waste reduction, careful attention must be given to the optimal dosage to balance environmental impact with structural performance. The study identified that low levels (≤5%) of RABCC incorporation could be beneficial for reducing waste without sacrificing CS. In contrast, higher levels may lead to undesirable reductions in strength, thus limiting the practical applicability of RABCC in structural concrete applications.

The current investigation was chiefly centered on the CS behavior and machine learning-based prediction of concrete containing RABCC. Consequently, it is important to recognize several constraints. Properties linked to durability such as water absorption, chloride penetration, sulfate resistance, shrinkage, freeze–thaw durability, and corrosion behavior were not experimentally assessed. Moreover, direct microstructural characterization methods, including SEM, EDS, XRD, and FTIR, were omitted; hence, conclusions regarding pore structure, bonding mechanisms, and ITZ behavior are currently inferential rather than direct. In addition, the machine learning algorithms were constructed from data derived from a single experimental series without the use of external independent validation datasets, potentially restricting the evaluation of wider applicability. Future studies should therefore emphasize thorough durability assessments, sophisticated microstructural examinations, enlarged multi-source experimental datasets, and external verification of predictive models across diverse environmental and field scenarios. Combining durability performance insights with explainable artificial intelligence and physics-informed machine learning approaches may enhance both the dependability and practical usage of RABCC concrete in sustainable construction projects.

Acknowledgement: Princess Nourah bint Abdulrahman University Researchers Supporting Project number (PNURSP2026R300). This study is supported via funding from Prince Sattam bin Abdulaziz University project number (PSAU/2026/R/1447).

Funding Statement: Princess Nourah bint Abdulrahman University Researchers Supporting Project number (PNURSP2026R300). This study is supported via funding from Prince Sattam bin Abdulaziz University project number (PSAU/2026/R/1447).

Author Contributions: Manish Kewalramani contributed to the conceptualization, methodology development, formal analysis, original draft preparation, and overall supervision of the study. Refka Ghodhbani participated in the experimental investigation, project administration, data interpretation, and manuscript revision. Arsalan Mahmoodzadeh contributed to the machine learning modeling, validation procedures, formal analysis, and manuscript writing. Abdulaziz Alghamdi and Abed Alanazi contributed to supervision, technical review, and funding acquisition. Faten Khalid Karim was involved in the experimental work, data collection, and analysis of concrete properties. Abdullah Alqahtani and Shtwai Alsubai contributed to data curation, visualization, and graphical preparation of the results. Mounir Ltifi contributed to the machine learning implementation, computational analysis, and manuscript editing. All authors reviewed and approved the final version of the manuscript.

Availability of Data and Materials: The datasets generated and/or analyzed during the current study are provided as Supplementary Material associated with this article. Additional information regarding the experimental database and machine learning implementation can also be obtained from the corresponding author upon reasonable request.

Ethics Approval: This study does not involve human participants, human data, or animals. Therefore, ethics approval was not required for this research.

Conflicts of Interest: The authors declare no conflicts of interest.

Supplementary Materials: The supplementary material is available online at https://www.techscience.com/doi/10.32604/cmes.2026.084696/s1.

References

1. Dizon P, Guanlao KLP, Marqueses KR, Oliva CJB, Aviso KB, Choi AES. Paving the way to sustainability: exploring the effects of additives on concrete mixes in enhancing mechanical properties and cost efficiency. Chem Eng Trans. 2025;120:151–6. doi:10.3303/CET25120026.

2. Marinković S, Carević V. Comparative studies of the life cycle analysis between conventional and recycled aggregate concrete. In: New trends in eco-efficient and recycled concrete. Amsterdam, The Netherlands: Elsevier; 2019. p. 257–91.
3. Kisku N, Joshi H, Ansari M, Panda SK, Nayak S, Dutta SC. A critical review and assessment for usage of recycled aggregate as sustainable construction material. Constr Build Mater. 2017;131(2):721–40. doi:10.1016/j.conbuildmat.2016.11.029.
4. Budziński B, Majer S, Cendrowski K, Rackiewicz W, Modrzejewski D, Zawidzki M, et al. Utilization of waste materials in cement-bound mixtures for sustainable construction. Sustainability. 2026;18(10):5066. doi:10.3390/su18105066.
5. Senaratne S, Lambrousis G, Mirza O, Tam VWY, Kang WH. Recycled concrete in structural applications for sustainable construction practices in Australia. Procedia Eng. 2017;180:751–8. doi:10.1016/j.proeng.2017.04.235.
6. Al-Alimi S, Yusuf NK, Ghaleb AM, Lajis MA, Shamsudin S, Zhou W, et al. Recycling aluminium for sustainable development: a review of different processing technologies in green manufacturing. Results Eng. 2024;23(8):102566. doi:10.1016/j.rineng.2024.102566.
7. Paktiawal A, Alam M. An experimental study on effect of aluminum composite panel waste on performance of cement concrete. Ain Shams Eng J. 2021;12(1):83–98. doi:10.1016/j.asej.2020.07.024.
8. Khai LTQ, Ha DNN. Recycled aluminum can fibers for concrete reinforcement: standardized testing of compressive strength and static elastic modulus. J Mater Const. 2025;15(2):31–5. doi:10.54772/jomc.v15i02.1179.
9. Othman PM, Herki BMA. Evaluation of the resistance of concrete to freezing and thawing containing recycled steel fibers and waste aluminum aggregates. J Comp Sci. 2026;10(4):183. doi:10.3390/jcs10040183.
10. Hafez RDA, Abd-Al Ftah RO. Utilization of waste aluminum fiber as a new fiber in high-strength concrete (HSC). J Umm Al Qura Univ Eng Archit. 2026:1–18. doi:10.1007/s43995-026-00295-5.
11. Mailar G, Sujay Raghavendra N, Sreedhara BM, Manu DS, Hiremath P, Jayakesh K. Investigation of concrete produced using recycled aluminium dross for hot weather concreting conditions. Resour Effic Technolog. 2016;2(2):68–80. doi:10.1016/j.reffit.2016.06.006.
12. Amanullayeva G, Aliyev S, Hasanova N. Development of new concrete composites based on various aluminum wastes. Eureka Phys Eng. 2025;6(6):45–53. doi:10.21303/2461-4262.2025.003958.
13. Makul N. Aluminum recycling waste. In: Dictionary of concrete technology. Singapore: Springer; 2025. p. 116–8.
14. Zhang M, Zhou K, Saunders T, Wang G, Wesling K, Liu J, et al. Low cost small scale recycling aluminium cans for energy conservation and environmental sustainability. Environ Technol. 2025;46(22):4575–82. doi:10.1080/09593330.2025.2509994.
15. Pereira AC. From can to sheet: a critical review of aluminum can recycling processes, technologies, and sustainability dimensions (2020–2025). Revft. 2025;29(151):19–20. doi:10.69849/revistaft/pa10202510261019.
16. International Aluminium Institute (IAI). Global aluminium statistics 2024. [cited 2025 Jan 1]. Available from: https://www.world-aluminium.org/.
17. United States Geological Survey (USGS). Mineral commodity summaries: aluminum 2024. [cited 2025 Jan 1]. Available from: https://www.usgs.gov/.
18. Verran GO, Kurzawa U. An experimental study of aluminum can recycling using fusion in induction furnace. Resour Conserv Recycl. 2008;52(5):731–6. doi:10.1016/j.resconrec.2007.10.001.
19. Barbhuiya S, Das BB, Adak D, Kapoor K, Tabish M. Low carbon concrete: advancements, challenges and future directions in sustainable construction. Discover Concr Cem. 2025;1(1):3. doi:10.1007/s44416-025-00002-y.
20. Siddiqui AR, Khan R, Akhtar MN. Sustainable concrete solutions for green infrastructure development: a review. J Sustain Constr Mater Technolog. 2025;10(1):108–41. doi:10.47481/jscmt.1667793.
21. Rusnak CR. Sustainable strategies for concrete infrastructure preservation: a comprehensive review and perspective. Infrastructures. 2025;10(4):99. doi:10.3390/infrastructures10040099.
22. Kara De Maeijer P. Innovative solutions for concrete applications. Infrastructures. 2025;10(3):59. doi:10.3390/infrastructures10030059.

23. Cuevas K, Strzałkowski J, Kim JS, Ehm C, Glotz T, Chougan M, et al. Towards development of sustainable lightweight 3D printed wall building envelopes—experimental and numerical studies. Case Stud Constr Mater. 2023;18:e01945. doi:10.1016/j.cscm.2023.e01945.
24. Shehzad A, Wang XX, Huang XH, Ullah K, Mohammad A, Althobaiti A, et al. AI-driven seismic optimization of outrigger systems in high-rise buildings: a machine learning framework for enhanced performance in earthquake-prone regions. J Build Eng. 2025;112(8):113864. doi:10.1016/j.jobe.2025.113864.
25. Momani Y, Tarawneh A, Alawadi R, Momani Z. Shear strength prediction of steel fiber-reinforced concrete beams without stirrups. Innov Infras Solut. 2021;7(1):107. doi:10.1007/s41062-021-00703-w.
26. Li Z, Bing Y, Chen S, El-Meligy M, Garayev M. On the measurement of resonance frequency of nanoclay-reinforced concrete shell structures validated by experimental datasets via artificial intelligence technique and mathematical modeling. Measurement. 2025;248(6):116961. doi:10.1016/j.measurement.2025.116961.
27. Mohamed HS, Qiong T, Isleem HF, Tipu RK, Shahin RI, Yehia SA, et al. Compressive behavior of elliptical concrete-filled steel tubular short columns using numerical investigation and machine learning techniques. Sci Rep. 2024;14(1):27007. doi:10.1038/s41598-024-77396-5.
28. Abbas YM, Babiker A, Ismail Ismail F. Optimized XGBoost-based framework for robust prediction of the compressive strength of recycled aggregate concrete incorporating silica fume, slag, and fly ash. Comput Model Eng Sci. 2025;145(3):3279–307. doi:10.32604/cmes.2025.074069.
29. Behnood A, Golafshani EM. Machine learning study of the mechanical properties of concretes containing waste foundry sand. Const Build Mater. 2020;243(4):118152. doi:10.1016/j.conbuildmat.2020.118152.
30. Penido RE, da Paixão RCF, Costa LCB, Peixoto RAF, Cury AA, Mendes JC. Predicting the compressive strength of steelmaking slag concrete with machine learning—considerations on developing a mix design tool. Const Build Mater. 2022;341(9):127896. doi:10.1016/j.conbuildmat.2022.127896.
31. Mai HT, Nguyen MH, Trinh SH, Ly HB. Toward improved prediction of recycled brick aggregate concrete compressive strength by designing ensemble machine learning models. Const Build Mater. 2023;369:130613. doi:10.1016/j.conbuildmat.2023.130613.
32. Han SH, Khayat KH, Park S, Yoon J. Machine learning-based approach for optimizing mixture proportion of recycled plastic aggregate concrete considering compressive strength, dry density, and production cost. J Build Eng. 2024;83(1):108393. doi:10.1016/j.jobe.2023.108393.
33. Golafshani E, Khodadadi N, Ngo T, Nanni A, Behnood A. Modelling the compressive strength of geopolymer recycled aggregate concrete using ensemble machine learning. Adv Eng Softw. 2024;191:103611. doi:10.1016/j.advengsoft.2024.103611.
34. Sahu A, Kumar S, Srivastava AKL, Pratap B. Machine learning approach to study the mechanical properties of recycled aggregate concrete using copper slag at elevated temperature. Asian J Civ Eng. 2024;25(1):911–21. doi:10.1007/s42107-023-00821-z.
35. Shoag M, Rahman MF. Using recycling aluminum cans as composite materials aluminum fiber. IOP Conf Ser Earth Environ Sci. 2021;943(1):012028. doi:10.1088/1755-1315/943/1/012028.